Journal of Materials Research and Technology 27 (2023) 4573–4594

Contents lists available at ScienceDirect

Journal of Materials Research and Technology

journal homepage: www.elsevier.com/locate/jmrt

Influence of low plasticity burnishing on the formation of strain induced martensite in the surface layer

Diogo Azevedo de Oliveira [a,*], Pedro Paiva Brito [a], Frederico de Castro Magalhães [b], Patrícia Canazart Azzi [c], José Domingos Ardisson [c], Alexandre Mendes Abrão [b]

[a] Graduate Program in Mechanical Engineering, Pontifícia Universidade Católica de Minas Gerais, Av. Dom José Gaspar, 500. Campus Coração Eucarístico, Belo Horizonte, 30535-901, Minas Gerais, Brazil
[b] Graduate Program in Mechanical Engineering, Universidade Federal de Minas Gerais, Department and Organization Antônio Carlos, 6627. Campus Pampulha, Belo Horizonte, 31270-901, Minas Gerais, Brazil
[c] Nuclear Technology Development Center (CDTN), Presidente Antônio Carlos, Rua Mário Werneck, 6627. Pampulha, Belo Horizonte, 31270-901, Minas Gerais, Brazil

ARTICLE INFO

Keywords:
Austenitic stainless steel
Low plasticity burnishing
Strain-induced martensitic
Surface deformation

ABSTRACT

In this research, AISI 304 austenitic stainless steel was used as work material and the influence of low plasticity burnishing (LPB) parameters (speed, number of passes and pressure) was investigated in terms of equivalent strain, LPB force, strain induced α'-martensite formation, deformation wave morphology and microhardness. Additionally, a correlation between the formation of α'-martensite and surface topography was investigated. The results showed that increasing the number of passes and pressure intensifies strain, while higher speed reduces friction and results in lower and more evenly distributed strain. The formation of LPB-induced α'-martensite was analyzed in a surface layer from 0.255 μm to a maximum depth of 2 μm. The highest content of α'-martensite was identified near the surface and decreased with depth. Mössbauer analysis (depth of ≈0.1 μm) supported this result. This behavior deviates from predictive models. Increasing the LPB speed reduces the α'-martensite content due to the generated adiabatic heat and, in some cases, its formation is nearly inhibited (< 5 %). The increase in the number of passes elevates the strain and, consequently, the α'-martensite content, with a maximum value approximately 90 %. Furthermore, the number of LPB passes was the only parameter to produces a refined grain layer. The increase in pressure elevates the strain, raising the content of α'-martensite. The trend of increasing α'-martensite content with higher numbers of passes and pressure was also observed in the context of waviness, i.e., the increase in deformation that is responsible for the higher α'-martensite content also increases the surface waviness.

1. Introduction

Low plasticity burnishing (LPB), deep rolling, deep cold rolling, ball or roller burnishing are terms used to refer to the same group of mechanical surface treatments that consist of plastically deforming the surface and subsurface of a metal or alloy, inducing compressive residual stresses [1,2]. They are extensively used aiming to increase the service life of components subjected to fatigue owing to the easiness of use and lower cost compared to thermal and thermochemical treatments [3]. LPB is widely applied in the aerospace [4,5], medical [6,7], nuclear [8] and automobile industries [9]. This process employs a ball that plastically compresses and deforms (through the action of hydrostatic pressure) the surface and subsurface of the work material during the relative movement between the part and the ball [10]. LPB can reduce the surface roughness by up to 35 times [11] and increase the fatigue strength by more than 200 % [12]. In AISI 304 austenitic stainless steel, deep rolling increases the uniform and localized corrosion resistance due to improved surface quality, grain refinement and induction of compressive residual stresses [13]. The mass loss due to cavitation erosion is also reduced when compared with non-burnished condition [14]. Intensive plastic deformation induces strain hardening in AISI 304 austenitic stainless steel and, as a result, leads to a substantial increase in surface hardness from 172 to 681 HV 0.1. Furthermore, deep rolling induces compressive residual stress near the surface, which results in improving the resistance to both fatigue crack nucleation and growth increases, thus elevating the low-cycle fatigue life in 250 % [15].

* Corresponding author.
E-mail addresses: diogoazev@yahoo.com.br, abrao@demec.ufmg.br (D.A. Oliveira).

https://doi.org/10.1016/j.jmrt.2023.10.133
Received 22 June 2023; Accepted 12 October 2023
Available online 20 October 2023

The properties of the materials subjected to LPB are strongly influenced by the operation conditions. The published literature concerned with the influence of the LPB parameters on the work material properties such as hardness, roughness, residual stresses, fatigue life, etc., is prolific. Table 1 presents selected research works that show the influence of speed, number of passes and pressure/force on the LPB outcome. These parameters will be discussed owing to their relevance to the present work.

The influence of speed on plastic deformation depends on the sensitivity of the material to the strain rate and, therefore, it may or may not be affected by speed. Sensitivity to strain rate is strongly influenced by temperature and, for most metals, has an almost negligible effect during cold deformation [25]. For this reason, the LPB speed is a parameter that has little or no influence on the responses material, as reported by Rodríguez et al. [17] and Chomienne et al. [16]. The reduction in the depth and intensity of residual stresses, microhardness and an increase in roughness observed by [18,20] attributes to the localized increase in temperature the possible recovery from work hardening at the surface of the work material, thus reducing the surface hardness with an increase in burning speed [19].

The influence of the number of passes is more evident than burnishing speed. In general, further increasing the number of passes promotes an increase in hardness and compressive residual stress [3]. Surface defects generated by previous machining operations are eliminated by the multiple passes that improve surface quality and induce the formation of short fatigue cracks instead of long cracks and retards crack propagation under cyclic loading, which explains the fatigue life improvement when compared to only machined components [15]. Such behavior can be attributed to the successive strain hardening of the material [21]. However, there is a tendency for saturation to a maximum strain limit due to the maximum deformation capacity of the material. Similar to burnishing pressure or force, excessive deformation can lead to surface and subsurface deterioration, with the inducement of cracks that lead to fracture [22].

The effect of increasing the normal burnishing pressure or normal force is similar to the effect of increasing the number of passes. This is because both parameters contribute to increase work hardening of the material. The result is the increase in intensity and depth of compressive residual stress and microhardness [2]. However, if the increase in pressure or normal force exceeds the ultimate strength of the material, cracks will be generated and lead to premature fracture [19]. The surface can be also deteriorated by increasing burnishing pressure [24], however, the roughness is always lower when compared to that generated by the previous the machining operation [17].

In the particular case of AISI 304 austenitic stainless steel, deformation can involve, in addition to work hardening, the formation of deformation twins, phase transformation induced by deformation and adiabatic effect. In this context, the influence of strain rate and strain state is more complex [26]. It can affect the burnished workpiece in different ways. Muñoz-Cubillos et al. [27] observed an increase in roughness when the DR speed increased approximately 60 %. The authors also observed that an increase in the deep rolling force promoted an increase in hardness and a decrease in roughness. This same behavior was observed by Maximov et al. [28], who pointed out that there is a limit to the increase in the burnishing normal force, from which the roughness increases and the hardness intensity is reduced. The improvement in the mechanical properties of AISI 304 austenitic stainless steel through LPB is mainly attributed to the formation of a complex microstructure composed of a refined grain layer with deformation bands, deformation twins, and a high dislocation density. However, the formation of martensite induced by plastic deformation is the main phenomenon responsible for the performance of this material after LPB [15,27,29,30].

In austenitic steels, there is a predominance of the α'-martensite phase which nucleates as stable embryos at micro-shear bands or twin-fault intersections [31]. The formation of α'-martensite can contribute

Table 1
Survey on influence of burnishing speed, number of passes and pressure on the LPB outcome.

Parameters				
Input	Levels	Work material	Findings	Ref.
Speed	10–100 mm/min	15-5 PH stainless steel	No significant variations between the values of residual stresses were found.	[16]
	75–150 m/min	AISI 1045 steel	No significant variations between the values of microhardness ans surface quality.	[17]
	500-150 mm/min	Magnesium alloy AZ31B	Reduction in the intensity and depth of compressive residual stresses at the highest simulated speed level along the burnishing direction. Increase in Ra and Rt values with increasing burnishing speed.	[18]
	5–48 m/min	Aluminum and brass	Increase in roughness and a reduction in hardness when speed was increased.	[19]
	63–160 m/min	Aluminum alloy 6061	Increase in Ra at speeds higher than 100 mm/min. The increase in the number of passes associated with the increase in speed impaired the surface quality, with Ra values increasing about three times.	[20]
Number of passes	1–3	Mild steel	Increase in microhardness when the number of passes was increased.	[21]
	1–5	Aluminum and brass	Reduction in Ra values and increase in microhardness when the number of passes was increased.	[19]
	1–6	Aluminum and brass	Reduction of surface roughness up to the first four passes, but roughness increased beyond this value. Increase in surface hardness with the increase in the number of burnishing tool passes.	[22]
	2 and 4	AISI D2 steel	Reduction of Ra and increase in microhardness when the number of pass was increased.	[15]
Pressure/ Normal force	20 and 30 MPa	AISI 1060 steel	Turning operation induced a residual tensile stress of 50 MPa that was converted to compressive stress, with an intensity of approximately −1100 MPa after LPB at a pressure of 20 MPa. Compressive stress reached a maximum intensity of −1730 MPa with an increase in pressure to 30 MPa.	[2]
	343–686 N	Aluminum and brass	Decreased mean roughness when normal burnishing force was increased up to a certain limit, beyond which roughness increase. Increased microhardness	[19]

(*continued on next page*)

Table 1 (*continued*)

Parameters				
Input	Levels	Work material	Findings	Ref.
			when normal burnishing force was increased.	
	15–25 MPa	AISI 1045 steel	Increase in microhardness with increasing pressure, reaching the maximum hardness value at 25 MPa (variation of approximately 110 HBN compared to machined samples). Pressure can also result in an increase in Ra.	[17]
	40–259 N	Low, medium and high carbon steel	The increase in normal force did not affect the surface quality of the low-carbon steel, but in steels with medium and high carbon content, the increase in force significantly reduced the Ra value.	[23]
	50–400 N	WE43 magnesium alloy	Normal burnishing force was the parameter that promoted the highest contribution (42.75 %) to surface quality. When pressure increased from 50 to 200 N, the workpiece surface peaks were flattened and the surface quality improved, however, an increase in normal force above 200 N impaired surface quality.	[24]

positively or negatively to the performance of the component, depending on its application. However, the transformation-induced plasticity (TRIP) effect is the most significant one for the application of these steels, which can be indicated here. Wang et al. [32] report that formation of α'-martensite decreases the aqueous corrosion resistance, reduces ductility and is detrimental to low-temperature nitriding. Briant e Ritter [33] state that plastic deformation reduces the time required for sensitization of AISI 304 and 316 austenitic stainless steels, but the effect is much more accelerated in AISI 304 steel, the only steel presenting strain-induced martensitic formation in the performed tests. This effect was attributed to the greater diffusivity of chromium and carbon in the body-centered tetragonal lattice (α'-martensite) than in the face-centered cubic lattice (austenite), thus reducing the temperature for the precipitation of chromium carbides which, as a consequence, promoted transgranular corrosion.

The findings by Eliezer et al. [34] suggest that hydrogen induced cracking requires the presence of stress induced α'-martensite in AISI 304 stainless steel. According to the authors, the diffusivity of hydrogen at room temperature in the BCC lattice is greater than that in the body-centered cubic (FCC) lattice, therefore, the martensite formed ahead of the crack can favor the diffusion of hydrogen. Such result is consistent with the crack propagation velocity in slow crack growth (SCG). From this study, it was concluded that the formation of α'-martensite decreases the ductility of austenitic steels and plays a crucial role in increasing the strength of austenitic stainless steels. In addition to the fact that the flow stress of α'-martensite is higher than that of austenite, it has a higher yield stress and is essential to sustain the strength of the material against necking under tension [35]. Nikitin and Altenberger [36] noticed that deep rolling induces the formation of a nanocrystalline layer, as well as the formation of α'-martensite, micro twins and high dislocation density near the surface. The authors conclude that, at elevated temperatures, the fatigue life of deep rolled specimens was longer than that of the laser-shock peened samples due to the more stable microstructure near the surface. In order to evaluate the effect of LPB process on hydrogen-assisted cracking of a martensitic stainless steel, Dreano et al. [37] found that burnished specimens presented higher elongation and much less secondary cracking when compared with the polished samples. The high compressive longitudinal stress induced near the surface is the main reason for the beneficial effect of LPB on the resistance of the hydrogen assisted cracking, which tends to inhibit crack nucleation and hence delays failure. In addition, a reduction of approximately 30 % in the amount of hydrogen introduced at the surface is expected due to the high compressive hydrostatic stress.

The published literature focused on the influence of the burnishing parameters on the properties and behavior of austenitic stainless steels is scarce, especially with regard to the formation of strain induced martensite. Understanding the influence of the LPB parameters on the strain induced martensitic formation is crucial, given the ambiguous influence of martensite on the behavior of the processed part. Therefore, this work aims to evaluate the influence of LPB parameters, namely speed, number of passes and pressure on the burnishing force, deformation wave formed ahead of the tool, formation of α'-martensite induced by plastic deformation and surface microhardness of AISI 304 austenitic stainless steel.

2. Materials and methods

AISI 304 austenitic stainless steel was selected as work material. Its chemical composition (see Table 2) was obtained by optical emission spectrometry – iron base in an optical emission spectrometer Spectromaxx.

After machining, samples with dimensions of 30 x 30 × 12 mm were solubilized in a muffle furnace (maximum temperature of 1200 °C) to inhibit the formation of carbides on the grain boundaries, thus ensuring the formation of austenite. Next, the samples were ground and polished. To perform the LPB tests, an Ecoroll hydrostatic tool was mounted on a machining center (maximum power of 9 kW) and ceramic balls with a diameter of 6.3 mm were used. The burnishing parameters are given in Table 3. The variation in the burnishing speed was of one order of magnitude to highlight the effect of strain rate. The number of burnishing passes (n) was varied in three levels (one, three and five). The maximum value of the number of LPB passes ($n = 5$) was established based on extensive literature [27,38–40], showing that more than five passes does not produce a significant effect on material properties. The burnishing pressure was applied in four levels, two of low intensity (16 and 24 MPa) and two of high intensity (32 and 40 MPa). A stepover of 0.1 mm with an overlap factor of 99 % was used [41] because the reduction in the stepover increases the burnishing overlap factor, thus diminishing the maximum height of the roughness profile (Rz) considerably [5,42]..

Fig. 1a presents the low plasticity burnishing experimental setup. The hydrodynamic action is performed by Petronas Mecafluid S3000 synthetic fluid (diluted in water at a concentration of 10 %) pumped from a high pressure pump and delivered to the LPB device. The ball is presses against the workpiece surface, thus promoting surface and subsurface plastic strain. The intensity of plastic strain depends on the applied hydrodynamic pressure, the work material and the contact area between the ball and the workpiece surface, the latter depending on the LBP parameters. After the initial surface deformation, the pressure is kept and the tool travel along the burnishing path (Fig. 1b) as determined by the CNC software (G code). According to the CNC machine coordinate system, the X, Y, and Z axes correspond to the stepover direction, burnishing speed direction, and burnishing force direction, respectively. All burnishing passes were performed on the same path. During the first burnishing pass ($n = 1$), the tool starts at point A and runs from point A to B, from B to C, from C to D, and follows the path until reaching the end point Z. For additional passes ($n = 2$ to 5), the tool returns to the start point (point A) and travels the path again. Using this

Table 2
Chemical composition of AISI 304 austenitic stainless steel (wt.%).

C	Mn	P	S	Si	Ni	Cr	N	Mo
0.0310	1.8339	0.0351	0.0225	0.4217	8.2724	18.1507	0.1115	0.6253

Table 3
Burnishing factors and levels.

Parameter	Values
Speed, V_b (mm/min)	10^2, 10^3 and 10^4
Number of passes, n	1, 3 and 5
Pressure, P (MPa)	16, 24, 32, 40

configuration, the sample is fixed on an auxiliar device mounted on a Kistler 9272 piezoelectric dynamometer, connected to a data acquisition board and computer.

The pin-on-disk tests were performed on a Micro Photonics Model MT 60 tribometer to determine the coefficient of friction between the burnishing ball and the stainless steel AISI 304, following the ASTM G99-05 standard [43]. The sliding speeds used in the pin-on-disk tests were the same used in LPB ($v_\mu = V_b = 10^2$, 10^3 and 10^4 mm/min) and the normal load was 5N. These results were used to feed the numerical model and are presented in Fig. 2. The average value of the coefficient of friction for sliding speeds of 10^2 and 10^3 mm/min, obtained in after running-in, were the same (approximately 0.27). Increasing the speed to 10^4 mm/min reduced the coefficient of friction to approximately 0.16.

The results obtained from the axial compression tests were employed as input data in the numerical simulation software to evaluate the mechanical behavior of the material during the LPB process. For this purpose, ten test specimens (and duplicates) were machined with cross-sectional dimensions of 8 × 8 mm and a height of 10 mm. The tests were performed at room temperature using an Instron 5582 machine with a maximum load capacity of 10 tons. To investigate the influence of strain rate on the material behavior, displacement speeds were varied across eight levels: 10, 35, 70, 100, 200, 300, 400 and 500 mm/min. The corresponding strain rates were: 0.018, 0.05, 0.085, 0.14, 0.28, 0.42, 0.56, and 0.69 s^{-1}. Fig. 3 illustrates one of the compression test results along with the strain rate curve.

The numerical simulation of the LPB was carried out using the finite element method (FEM), namely Ansys Workbench module (2008). Fig. 4 shows the proposed numerical model with boundary conditions (Fig. 4a), where the ball cage and the ball are considered rigid bodies (high elastic modulus). To describe the mechanical behavior of the work

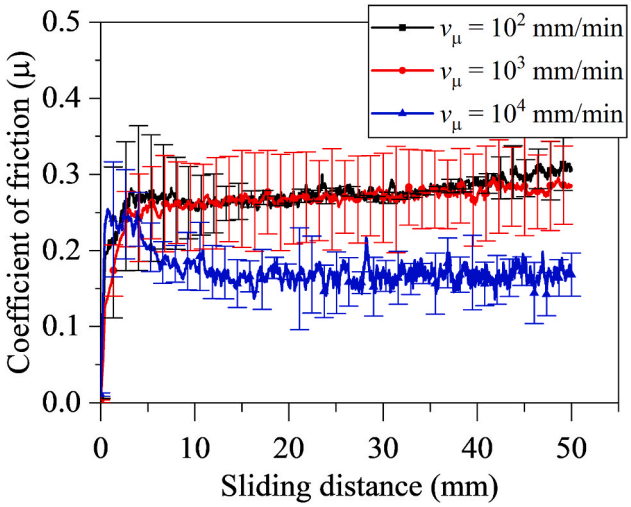

Fig. 2. Coefficient of the friction for sliding speeds of 10^2, 10^3 and 10^4 mm/min.

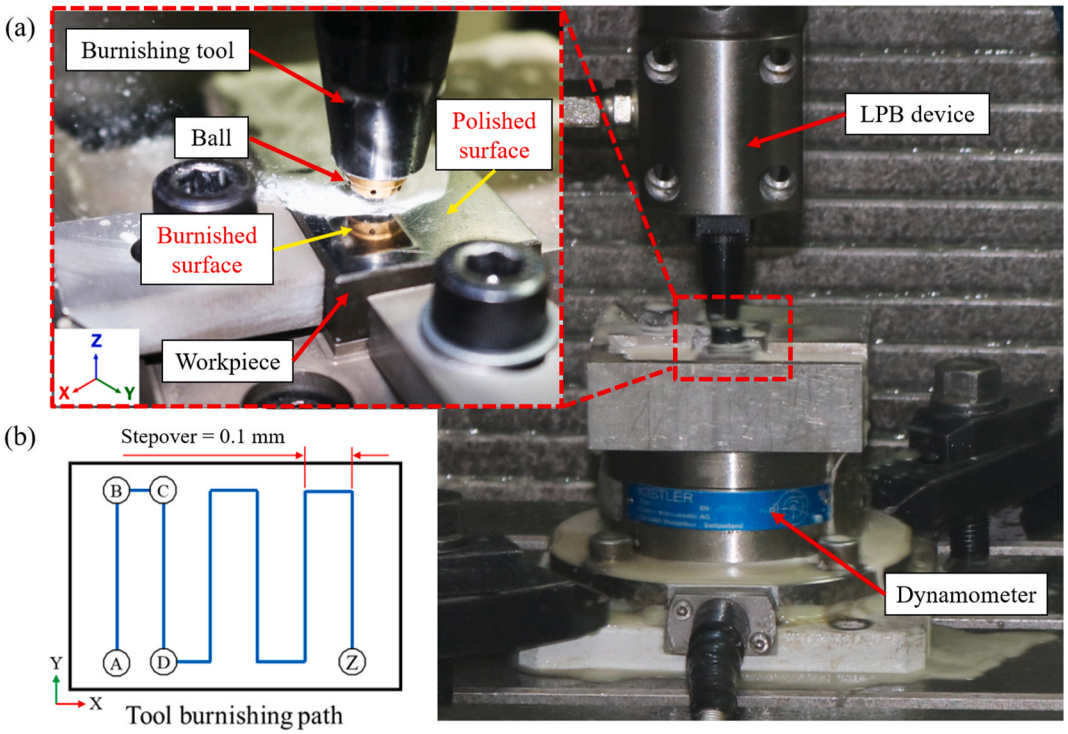

Fig. 1. Low plasticity burnishing: (a) experimental setup and (b) burnishing tool path.

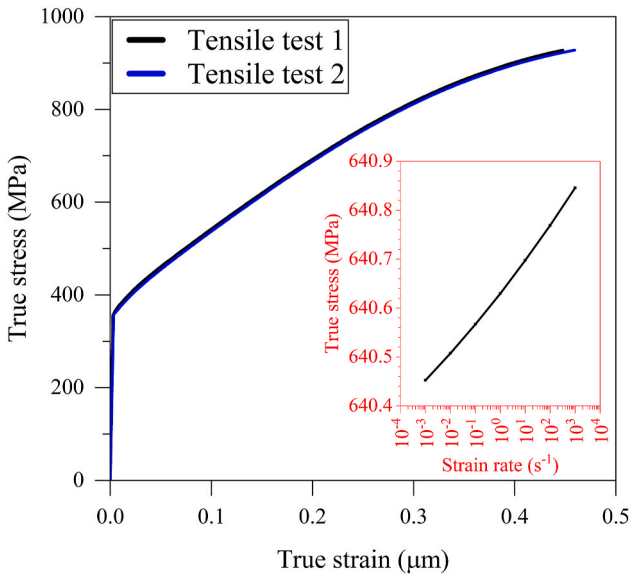

Fig. 3. Compression test results highlighting the effect of strain rate.

material, elastic and plastic regimes were considered (Fig. 3). Axial compression tests were performed to determine the yield stress. The adopted numerical model was used to determine strain only and was not able to predict strain induced phase transformation. Thermal effects were neglected. In terms of restrictions to the movement of the bodies involved, the lower surface of the material was considered completely stationary ($V_x = V_y = V_z = R_x = R_y = R_z = O$) and the other surfaces of this work material presented translation and rotation movements in all directions ($V_x \neq V_y \neq V_z \neq R_x \neq R_y \neq R_z \neq O$). Taking into account that LPB promotes localized and highly intense plastic deformation on the surface of the work material, second-order hexahedral elements were used to discretize the material, having elements with smaller dimensions in the region to be burnished. Rigid bodies were discretized with first-order hexahedral elements with dimensions of 0.2 mm. To reproduce the effect of the layer of fluid surrounding the ball and preventing its contact with the cage, the coefficient of friction was considered null between the cage and ball. In order to reliably preserve the rotation and sliding movements of the ball, the degrees of freedom for translation and rotation in the X, Y and Z axes of the ball inside the cage were considered free. The Coulombian friction model was used to describe the contact between the ball and the work material, based on the results obtained in the pin-on-disc tests (Fig. 2). The sliding friction between the ball and the material is concomitant with the linear movement of the cage together with the pressure exerted by the ball on the material. To establish an initial contact, compression of the ball against the work material in Z axis direction was considered until reaching the values of the forces measured experimentally for the respective pressures of 16 and 40 MPa. The numerical evaluation of the equivalent total strain was carried out in six stages along the tool path. Thus, the tool starts the burnishing path at point A to point B (completing stage 1), then moves 0.1 mm in the step-over direction (X axis) to point C and continues in the

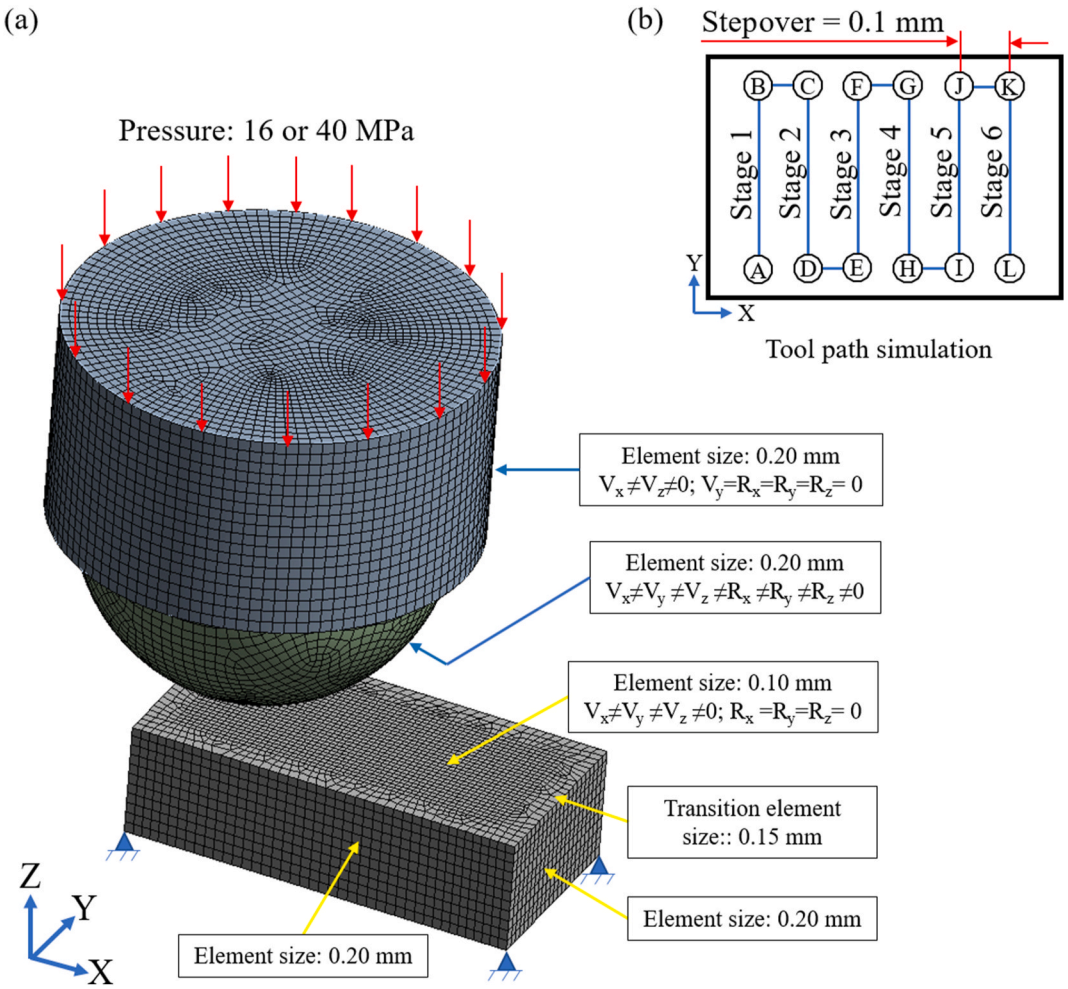

Fig. 4. FEM setup: (a) boundary conditions and (b) simulated tool path.

burnishing direction to point D (completing stage 2), and so on to point L (completing stage 6), as shown in Fig. 4b. For the numerical simulation, the influence of the burnishing speed on the equivalent total strain was evaluated between the extreme levels tested (10^2 and 10^4 m/min) with constant pressure and number of passes (P = 16 MPa and $n = 1$). The influence of the number of burnishing passes was evaluated in the first and third level ($n = 1$ and $n = 3$) with constant values of speed (10^2 m/min) and pressure (P = 16 MPa). Finally, the influence of burnishing pressure was evaluated between its extreme levels of 16 MPa and P = 40 MPa with constant values of speed (10^2 m/min) and number of passes ($n = 1$).

A Hommel Etamic T8000 contact profilometer with a Tku 300/600 pick-up with a diamond stylus (90° and 5 μm radius) was used to obtain the surface topography data. MountainsMap software was employed to process the following data: arithmetic mean waviness (Wa), which corresponds to an average of 20 roughness profiles and roughness patterns through continuous wavelet transform (CWT). The continuous wavelet transform (CWT) is suitable for analyzing profiles with non-stationary characteristics, such as those generated by plastic deformation. This analysis emerged as an alternative to the Fourier transform, providing long time and low frequency resolutions to high frequencies, and high frequency and short time to low frequencies [44].

The X-ray diffraction analyses were performed at room temperature in a Rigaku Ultima IV diffractometer. To keep the geometries permanently assembled and aligned, a Cross Beam Optics (CBO) system with parallel beam slit was attached to the light output. Grazing incidence X-ray diffraction (GIXRD) tests were performed to identify and quantify the phases formed just beneath the burnished surface (< 2 μm). The test conditions were as follows: incident radiation with Cu Kα ($\lambda = 1.5418$ Å) anode, scattering angle ranging from 42° to 46° (θ-θ), grazing incidence angle (α) ranging between 1° and 8°, step of 0.02°, goniometer speed of 0.4°/min, current intensity of 40 mA and voltage of 40 kV. The martensitic fraction was obtained by Rietveld refinement using MAUD software. The austenite (code AMCSD 0015352) and α'-martensite (code AMCSD 0015337) CIF files were obtained in Crystallography Open Database [45] and their respective lattice parameters are 3.639 and 2.878 Å, respectively. The martensitic content was obtained as a function of the diffracted depth, which in turn depends on the grazing incidence angle [46]. The diffracted depth (P_d) corresponds to the inverse of the linear absorption coefficient (μ), see Eq. (1):

$$P_d = \frac{1}{\mu} \tag{1}$$

The linear absorption coefficient can be obtained from the mass absorption coefficient (μ_m) and the density (ρ) of each chemical compound can be calculated, according to Eq. (2):

$$\mu = \mu_m \cdot \rho \tag{2}$$

In a mechanical mixture, solution or chemical compounds, whether in the solid, liquid or gaseous states, the linear absorption coefficient can be obtained by the weighted average between the mass absorption coefficient of all elements as a function of the weight fraction of the elements of the material (w), as represented in Eq. (3):

$$\frac{\mu}{\rho} = w_1\left(\frac{\mu}{\rho}\right)_1 + w_2\left(\frac{\mu}{\rho}\right)_2 + w_3\left(\frac{\mu}{\rho}\right)_3 + \cdots \tag{3}$$

Finally, the diffraction depth for incidence angle at 63 % ($P_{d63\ \%}$) of the measured intensity is given by Eq. (4):

$$P_{d63\%} = \frac{1}{k\mu} = \frac{\sin(\alpha)\sin(2\theta - \alpha)}{\mu[\sin(\alpha) + \sin(2\theta - \alpha)]} \tag{4}$$

The HighScore Plus software [47] was used to calculate the diffracted depth, considering the respective mass absorption coefficients from the chemical composition of AISI 304 stainless steel: Cr (252.76 cm^2/g), Ni (48.51 cm^2/g), Mn (278.13 cm^2/g), Si (62.07 cm^2/g), N (7.09 cm^2/g), C (4.30 cm^2/g), P (74.30 cm^2/g), S (89.70 cm^2/g) and Fe (310.94 cm^2/g) and atomic packing factor of the FCC lattice (0.74).

Mössbauer spectroscopy is a nuclear spectroscopy with energy resolution capable to resolve hyperfine structures at nuclear level [48]. Spectrum generated by the conversion electron Mössbauer spectroscopy (CEMS) technique can be obtained by the integral technique, in which all electrons leaving the surface are collected, or by the differential or depth selective CEMS technique, in which electrons with a certain energy range are selected by means of a beta-ray spectrometer [49]. The Mössbauer spectrum is characterized by the shapes, intensity, position and number of the several absorption lines that constitute the spectrum. The intensity, for instance, depends on the concentration of the Mössbauer nuclei in the absorber. Nuclear hyperfine interactions are the disturbances caused in nuclear energy levels due to interactions between nuclear moments and electric and magnetic fields, created by charges close to the nucleus. The main hyperfine interactions observed by Mössbauer spectroscopy are:

i) isomeric deviation (&), which is a result of the electric monopole interaction between the nuclear charge distribution and the electronic charge density in the nucleus. The s electrons have the ability to penetrate the nucleus (they have zero angular momentum), and electrostatically interact with the nuclear charge. This interaction causes a displacement of the nuclear energy level &E, both in its fundamental and excited states;
ii) Electric quadrupole interaction, which splits nuclear energy levels with nuclear state I > 1/2 into doubly degenerate substates and leads to the electric quadrupole splitting (QS). In many nuclei the charge distribution deviates from the symmetrically spherical distribution. The measure of the deviation of the charge distribution is characterized by the electric quadrupole moment Q, which is a second-order tensor with elements. Q is positive for elongated nuclear charge distribution, negative for flattened distribution, and zero for spherical charge distribution. Quadrupole splitting can provide information about the electronic population of the orbitals, the structure of the ligand, among others;
iii) Magnetic dipole interaction, which splits nuclear energy levels that have nuclear state I > 0 into sublevels, with the degeneracy fully lifted. Magnetic interactions are observed in ferromagnetic, antiferromagnetic, and ferrimagnetic compounds and in paramagnetic systems, when the spin relaxation time (change in nuclear neighborhood with time or change in spin direction) of the electron is long. Among the three interactions, this is the only one that can be modified by an external variable.

The hyperfine magnetic field B_{hf} and the quadrupole interaction of the core are the most important parameters. The hyperfine field is related to the magnetic moment of the unfilled 3d or 4f layers. The quadrupole interaction is related to the electric field gradient in the nucleus, V_{ij} created by the unfilled 3d and 4f layers, and the potential due to all other charges. The hyperfine field, to a first approximation, is considered proportional to the magnetic moment according to Eq. (5):

$$B_{hf}^T = A_{hf} \cdot m_T \tag{5}$$

where A_{hf} is the hyperfine interaction constant (Fe = 15T/μ_B).

Mössbauer spectroscopy is a useful technique based on ^{57}Fe to estimate the local magnetic moment of Fe ions. However, assuming that m_T is proportional to B_{hf}^T is questionable in Eq. (1). The effective hyperfine field contains several contributions and can be written according to Eq. (6):

$$B_{hf}^T = B_{cp} + B_{cond} + B_{orb} + B_{dip} \tag{6}$$

Where B_{cp} and B_{cond} represent the contribution of core and conduction electrons. The spin polarization of the B_{cond} conduction electrons and the core electrons contribute differently to the B_{hf}. The B_{cp} term is proportional to the 3d spin moment, which is −13.8T/μ_B for Fe[17]. The

term B_{cond} is mainly due to the 4s polarization, which is sensitive to charge transfer. The other two terms are proportional to the orbital momentum (B_{orb}) and the dipole field (B_{dip}).

Conversion electron Mössbauer spectroscopy (CEMS) was used to identify the phase transformation at a depth of less than 0.1 μm. The Mössbauer spectra of the sample surface were obtained in backscatter geometry at room temperature, using a ^{57}Co source in an Rh matrix using two different CEMS techniques, which detect two different species. The experimental data were adjusted by Lorentzian functions using least squares method and, for this purpose, the NORMOS-90 software [50] program was employed.

Ultra-microhardness tests were performed on a Shimadzu DUH-W201S ultra-microhardness tester with a Berkovich indenter, applying a step load-unload loading mode (speed of 5 s). This is a highly accurate method of measuring the depth of indentation, in which the specimen indentation depth can be measured in with a resolution 0.0001 μm. The ultra-microhardness value (H) obtained is a ratio between the maximum loading (P_{max}) of the indenter and the projected area of the indented impression (A_c). The contact area is calculated as a function of the contact depth (h_c), according to Eq. (7).

$$H = \frac{P_{max}}{A_c} = \frac{P_{max}}{24.5 \cdot h_c^2} \tag{7}$$

The applied forces were 98.5; 191.6; 286.4; 383.1; 477.7; 573; 667.6; 762.4; 857.2; 952 and 1046.7 mN. The holding times were 2 and 15 s for force application and indenter, respectively. For each sample, 20 measurements were performed. The microhardness curves were corrected according to the work proposed by Gong et al. [51].

Microstructure analyses of the cross sections of the burnished samples were carried out using the Electron Back Scattered Diffraction (EBSD) by a Scanning Electron Microscope (SEM) Quanta FEI-200, employing a step-size of 810 nm and ATEX software for data processing [52].

3. Results and discussions

3.1. FEM analysis

Fig. 5 presents the results of equivalent total strain for stages 1, 3 and 5 (shown in Fig. 4b) of the sample burnished with a pressure of 16 MPa, speed of 10^2 mm/min and one burnishing pass. For this analysis, a cross section of the sample is presented in order to evaluate the distribution of strain on the surface and subsurface. It can be seen is that in the contact region between the ball and the workpiece, deformation is heterogeneously distributed along the subsurface. This is due to the friction deformation wave between the ball and workpiece that alters the flow of material on the contact surface and, consequently, the surface strains. These strains increase and reach their maximum intensity in the subsurface of the workpiece, as established by the Hertz elastic contact model [53]. However, a "wave" is formed on the right side of the ball, in stepover direction. This deformation wave is the result of material flow during plastic deformation, which equivalent total strain intensity is almost as high as that recorded in the subsurface. Such behavior is not predicted by the strain distribution models, since these are very simplified models [10,54]. Albeit more sophisticated and with good predictability, other models also neglect some parameters or phenomena of the LPB/DR process [55,56]. Therefore, it is critical to understand the deformation process that induces phase transformation on the surface of the workpiece, since the deformation is the driving force for the occurrence of this phenomenon. The deformation wave begins to be formed in the first burnishing stages without full contact between the wave and the burnishing ball because, as previously mentioned, the

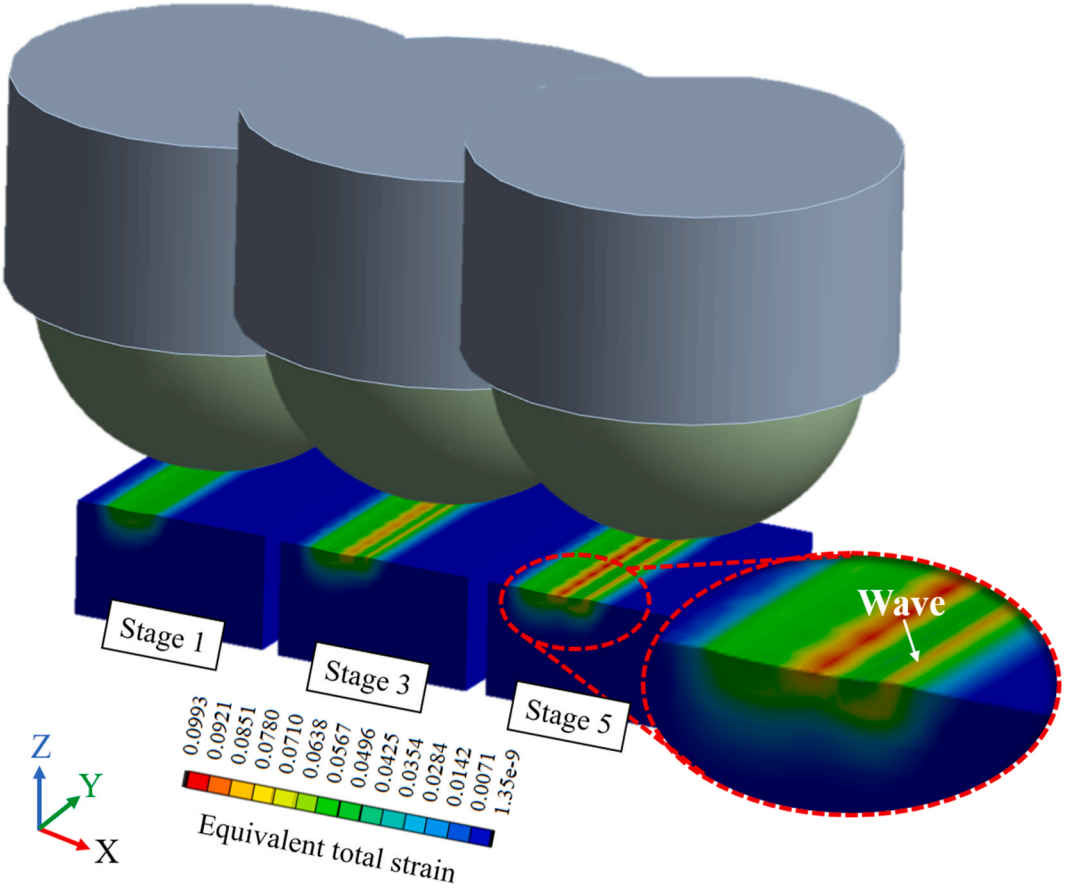

Fig. 5. FEM analysis of equivalent total strain (P = 16 MPa, $V_b = 10^2$ mm/min and $n = 1$.

wave is formed on the side of the ball, similarly to the indentation process. Once formed, the tool moves on to the subsequent stages and deforms the wave again, thus causing a further increase in surface strain. The numerical result suggests that the main source of strain responsible for inducing the phase transformation by surface strain results from this behavior.

3.1.1. *Influence of the burnishing parameters on the equivalent total strain on the surface*

Fig. 6a to c shows the evolution of the equivalent total strains stages 1–6 (left) are undertaken, together with the spatial distribution of these strains on the surface (right). Stages 1 and 6 represent, respectively, the beginning and end of LPB simulation. The influence of burnishing speed for a pressure of 16 MPa and one pass is shown in Fig. 6a. Note that not only is the strain intensity at the speed of 10^4 mm/min slightly lower compared to the speed of 10^2 mm/min, but so is the deformed area. Lower friction possibly promoted larger homogenization of strains, which should have increased surface strains. However, tribological contact conditions (e.g., the stick-slip phenomenon) may have influenced the deformation process resulting in the decrease of strains, since the model used did not predict the influence of thermally activated mechanisms. Even though the deformation is lower at the highest speed, its homogeneity favored the distribution of the strains in the wave formation region, as seen in the detail of Fig. 6. Although the equivalent total strain increased throughout the subsequent stages, the results suggested a strain saturation from stage 4 for both speeds, i.e., the wave was subjected to the highest possible deformation under the simulated conditions. The influence of the number of burnishing passes for a pressure of 16 MPa and speed of 10^2 mm/min is presented in Fig. 6b. Increasing the number of burnishing passes from one to three almost doubled the equivalent total strain values. Undoubtedly, an additional increment in the number of passes is expected to result in an elevation of the strain amplitude [19], however, it is critical to emphasize that the impact of this increment is attenuated due to the saturation of strain hardening [27]. For both one and three passes, the strain also saturated from the fourth stage. The distribution of surface deformation (right) showed that the deformed area increased considerably in the second pass. The influence of burnishing pressure (for samples simulated with a speed of 10^2 mm/min one pass) is shown in Fig. 6c. The increase in pressure increased the equivalent total strain on the surface and, according to [57], this behavior is expected. The strain saturation for the simulated sample with a pressure of 40 MPa showed a different behavior

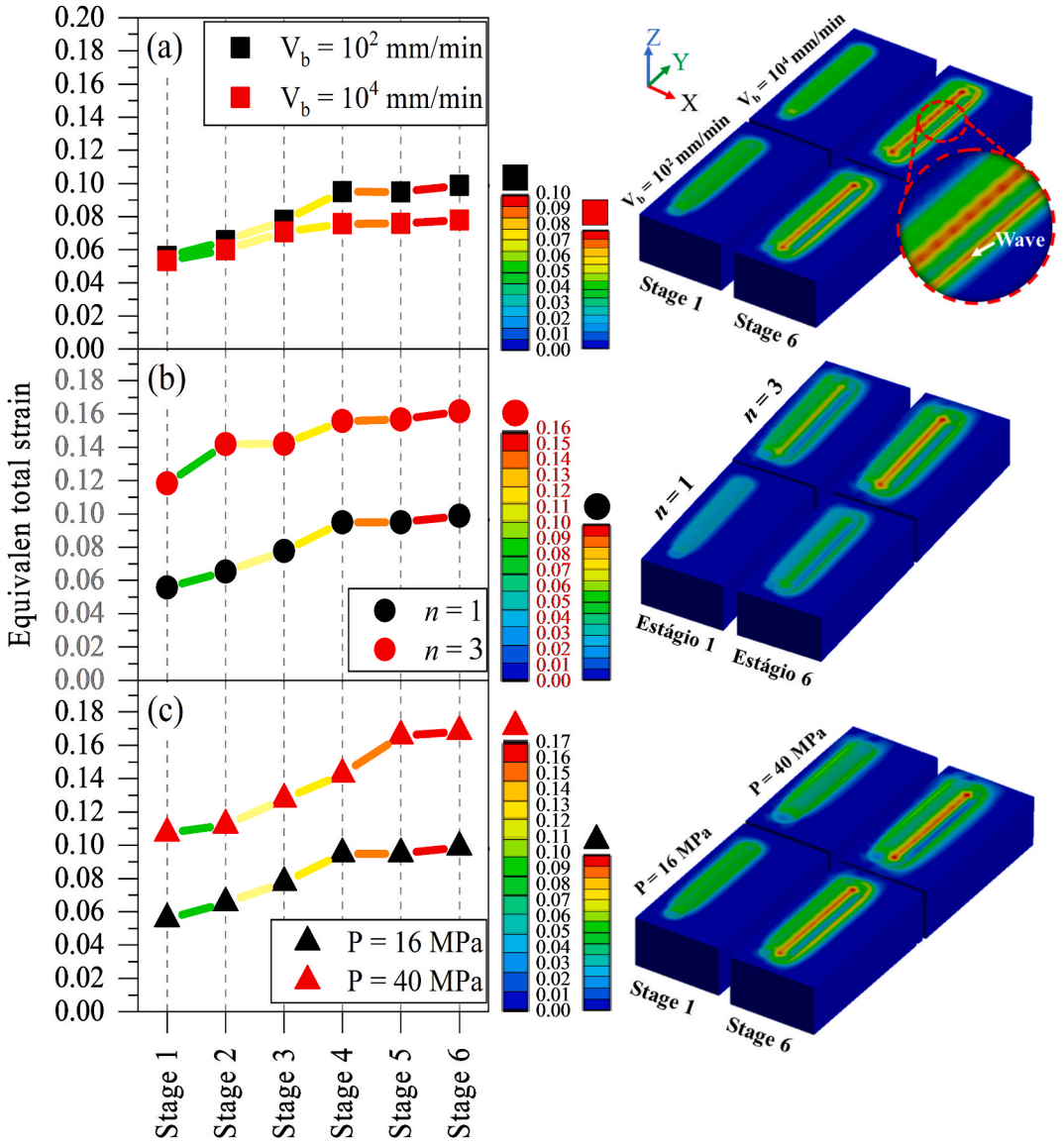

Fig. 6. FEM analysis: influence of the (a) burnishing speed (P = 16 MPa and $n = 1$), (b) number of passes (P = 16 MPa and $v_b = 10^2$ mm/min) and (c) pressure on equivalent total strain ($v_b = 10^2$ mm/min and $n = 1$).

from that observed in previous analyses. There was a delay in saturation, which occurred from the fifth stage. Furthermore, the difference in strains between the two pressure values increased from the fourth stage, thus indicating the higher severity of the deformation process under high pressures. In general, the number of burnishing passes and the pressure were the parameters that most affected the equivalent total strain.

3.2. Influence of the LPB parameters on the burnishing force

An statical analysis was performed in order to assess the influence of speed, number of passes, and pressure on the burnishing force. The results presented a normal distribution, with most residuals ranging between 20 and -20 (as a function of the fitted values) and mean around zero. The Tukey's test checks whether there is a statistically significant difference between the means of the response variables as a function of the factor levels. Thus, it can be stated whether the variation in the levels of a factor affects the output. For this difference to exist at a 95 % confidence level, the adjusted P-value must be equal to or lower than 0.05. Increasing the burnishing speed from 10^2 to 10^3 mm/min and the number of passes from three to five provided adjusted P-values of 0.075 and 0.201, respectively, indicating that changing these levels did not promote any remarkable variation in the burnishing force. For the remaining factors, varying the levels significantly affected the burnishing force. The analysis of variance indicated that the burnishing pressure is the most influential factor (contribution of 59.98 %),

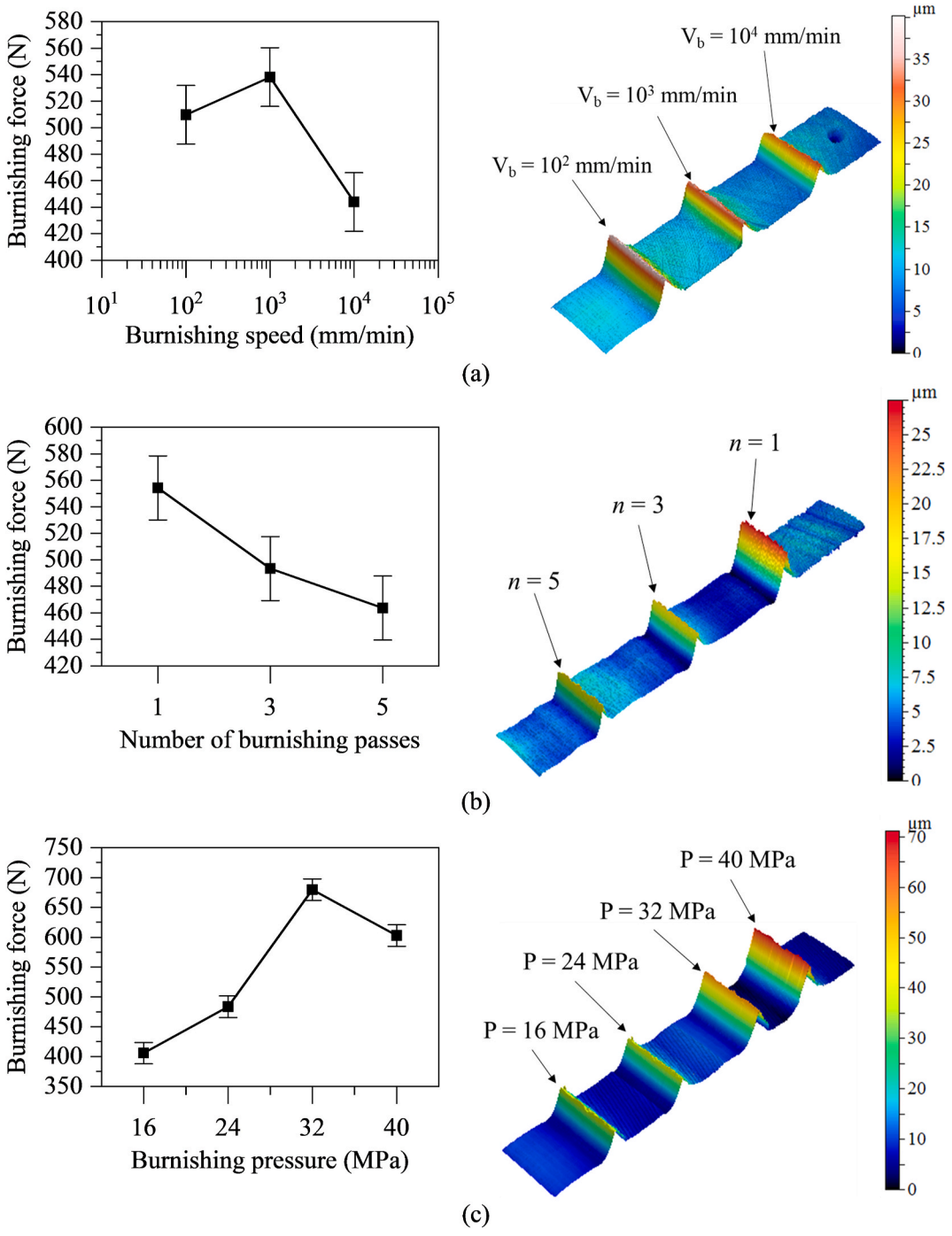

Fig. 7. Influence of (a) speed, (b) number of passes and (c) pressure on the burnishing force (left) and corresponding deformation wave (right).

followed by speed (12.19 %) and number of passes (9.59 %). Fig. 7 shows the influence of burnishing speed, number of passes and pressure on the burnishing force (on the left) and the height of the deformation wave (on the right).

Fig. 7a shows that an increase in burnishing speed from 10^2 to 10^3 mm/min did not promote a significant variation in burnishing force, however it considerably lower when burnishing was performed at 10^4 mm/min. The same behavior was noticed for the height of the deformation wave. The LPB device applies a constant force that depends on the pressure (16, 24, 32 and 40 MPa in the present work), but the burnishing force is the result of the contact stresses between the sphere and the workpiece. Such stresses depend, additionally to the force applied by the equipment, on the burnishing parameters, the fluid used, the materials involved, etc. In general, any aspect that changes the tribological conditions in the ball-workpiece contact tends to change the contact stresses and, consequently, the burnishing force. Increasing the speed to 10^4 mm/min produced a considerable reduction in the coefficient of friction from 0.27 to 0.16 (see Fig. 2), which may explain the reduction in the burnishing force. This reduction in the coefficient of friction can be the result of structural changes in the material that affected the contact conditions between the ball and the workpiece, as seen by the numerical simulation in Fig. 6a. Rolling is the main movement of the ball on the workpiece surface and friction between ball and workpiece will take place during material flow caused by plastic deformation. A high deformation wave increases the contact area between the ball and the work material surface, elevates the influence of friction that restricts plastic flow from the workpiece over the ball surface, causing instability during the process, as well as increasing the burnishing force [58]. Increasing the speed slightly reduced the coefficient of friction and the equivalent total strain and, consequently, the height of the deformation wave, i.e., it reduced the contact area between the ball and the workpiece, which is one of the reasons for the reduction in the burnishing force of approximately 15 %. An excessively high burnishing speed considerably reduces the contact time between ball and the work material surface and possibly decreases plastic deformation of the material. As mentioned in subsection 3.1 the tribological contact conditions were probably altered by the highest burnishing speed. The analysis of the friction coefficient between this tribological pair needs to be further explored, especially in the running-in phase, which can provide conclusive differentiation of speed-related phenomena. The tribological effect of LPB at High speed is an extremely complex condition, difficult to be accurately predicted by empirical methods and numerical simulation, and needs to be validated experimentally and numerically.

Fig. 7b shows the effect of number of passes on the burnishing force and height of the deformation wave. It can be seen that the burnishing force is reduced to approximately 11 % when the number of passes increases from one to three, and by 17 % when the number of passes is further increased to five. The height of the deformation wave is strongly affected by the number of burnishing passes. During the first pass, the burnishing ball deforms the work material in its original state (no strain hardened) and the deformation wave reaches a height of 30 μm to decreases to 17 μm with five passes, as seen in Fig. 7b. This is due to the successive work hardening steps that the material undergoes in each burnishing pass, which reduces its deformation ability. The tendency to the strain hardening saturation when the number of passes is increased results in elastic deformation only [27]. One must bear in mind that during LPB, plastic deformation is restricted to the surface and subsurface layers, i.e., it is a localized deformation without macroscopic deformation. It can be noted that the height of the deformation wave reduces from approximately 30 μm after one pass to 15 μm after five passes. Consequently, the contact area between the ball and the workpiece surface (with the deformation wave) is reduced by less than half. Analogously to the effect of the highest speed indicated by the numerical simulation (see spatial distribution of the strains in Fig. 6a), the reduction in the height of the deformation wave facilitates plastic flow because it reduces the effect of friction, resulting in a more homogeneous deformation.

Fig. 7c represents the influence of pressure on the burnishing force and height of the deformation wave. Increasing the pressure from 16 to 24 MPa elevated the burnishing force to 20 %. A further increase in pressure to 32 MPa raised the burnishing force to approximately 42 %, reaching its maximum value, to be subsequently reduced to 12 % when a pressure of 40 MPa is applied. The increased pressure provides an additional driving force for plastic deformation, thus increasing the height of the deformation wave. The highest deformation wave is found at 40 MPa, even with reduced burnishing force. The reduction in the burnishing force may be due to localized defects, such as the wave deforming over itself, as reported by Salahshoor and Guo [59], and the consequent generation of microcracks. Fig. 8 presents the influence of the burnishing pressures of 40 MPa ($V_b = 10^2$ mm/min e $n = 1$) on the burnished surface, highlighting the before mentioned defect generated by the wave deforming on itself (detail "A").

3.3. The influence of LPB on the formation of α'-martensite in the surface layer

Fig. 9 shows the GIXRD pattern of the control sample (not burnished) indicating only austenite (γ) peaks.

The near-surface analyses (depth < 2 μm) of the samples burnished with the pressure of 16 MPa (Fig. 10) indicated that LPB induces the formation of α'-martensite and its highest fraction occurs on the surface. For low pressure, the penetration of the ball into the material to be burnished is lower, resulting in low plastic deformation that, associated with the friction effect, inhibit the flow of material and, consequently, the formation of the wave, as observed in Fig. 6c. This effect further reduces the formation of α'-martensite because the strain near the surface tends to zero. The conditions that hinder the formation of α'-martensite refer not only to LPB, but also to the characteristics of the studied material. According to Nikitin and Altenberger [36], the temperature for complete inhibition of martensite transformation induced by plastic strain in AISI 304 austenitic stainless steel is approximately 50 °C. In fact, α'-martensite was formed under all the tested LPB conditions. The Md30 parameter obtained from [60] and calculated using the chemical composition presented in Table 2, indicated a maximum temperature of 10.4 °C. This result indicates that, under the conditions tested, LPB induced a true plastic strain higher than 30 %, which is a high value for the investigated process. Even with these restrictions, it was noted that LPB induced the formation of α' martensite near the burnished surface with a fraction up to 80 % at room temperature. Therefore, two aspects must be emphasized: the first refers to the deformation wave formed on the side of the ball and that is continuously deformed by the tool (see Figs. 6 and 7). This shows that deformation also occurs on the side of the burnishing tool and the wave that forms is deformed along the path as the stepover progresses, but due to the strain hardening (Fig. 6), the equivalent total strain tends to saturate, as seen in numerical simulation results. The second aspect is concerned with the multiaxial strain state associated with LPB, which generates more deformation bands intersections compared with uniaxial tension, which is preferential site for nucleation of α'-martensite [31].

For the Mössbauer spectroscopy analysis, two samples were randomly chosen. The purpose was to identify the phase transformation as close as possible to the surface, since this technique allows to a analyze a depth of less than 0.1 μm. Fig. 11a and b shows, respectively, the spectra of sample 1 (burnished with P = 32 MPa, $V_b = 10^3$ mm/min and $n = 1$) and sample 2 (burnished with P = 40 MPa, $V_b = 10^4$ mm/min and $n = 5$). The spectra obtained from Mössbauer spectroscopy were fitted with two and/or three sets of subspectra (sextets, doublets and singlets) which were associated with the γ-austenite (green line/singlets) and α'-martensite (red line/sextets) [61–63]. For both samples, α'-martensite formation was identified very near the surface. Although

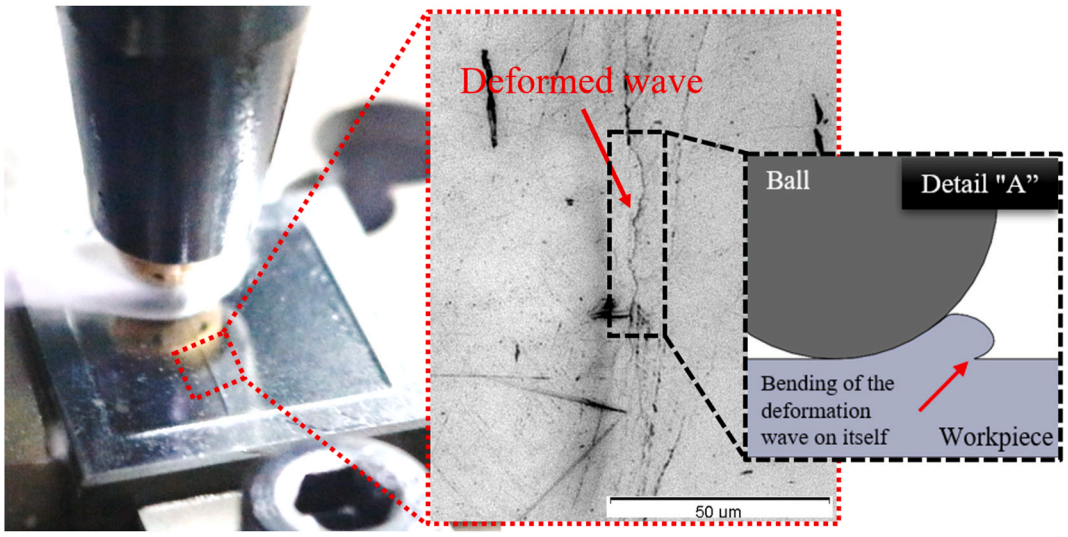

Fig. 8. Defect generated by burnishing pressures of 40 MPa on the burnished surface ($V_b = 10^2$ mm/min and $n = 1$).

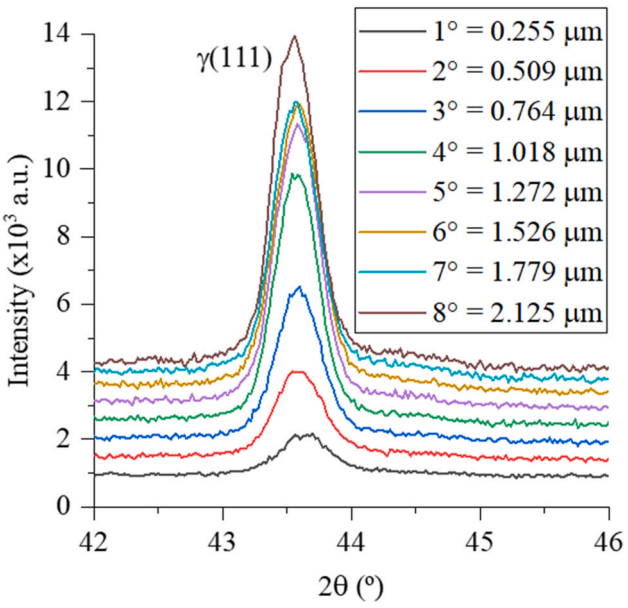

Fig. 9. GIXRD pattern of the control sample (no burnishing) with the calculated diffracted depths.

the presence of expanded austenite (ϵAE) was identified on Fig. 11b, this aspect will not be addressed as it is not the focus of this research and further analysis must be conducted before discussing this phenomenon.

Table 4 presents the hyperfine parameters of the Mössbauer spectroscopy (CEMS) analyses for samples 1 and 2 and the α'-martensite contents were 45 % and 59 %, respectively. Fig. 12 presents the results for the amount of α'-martensite formed as a function of the depth (< 2 µm) of the surface layer affected by LPB.

This analysis aims to evaluate the tendency to martensite formation on the surface layer. For this purpose, the results obtained by GIXRD at depths from 0.255 to 2.125 µm were used to generate an empirical model that describes the behavior of martensite content as a function of depth. For samples 1 and 2. Eqs. (8) and (9), respectively, describe such behavior with $R^2_{adj.} = 0.99$. Curves 1 and 2 were extrapolated to a depth of 0.1 µm and presented α'-martensite fractions equivalent to 44.44 % and 58.55 %. As seen in Fig. 12, for the same depth, the Mössbauer spectroscopy analysis indicated martensite fractions equivalent to 45 % and 59 %, respectively. The values obtained empirically and by extrapolation of the curves were very close (maximum difference less than 0.56 %), therefore, for a surface layer up to 2 µm depth, it can be stated that there is a tendency for an increase in the fraction of martensite up to the surface. Since this martensite is formed by deformation, by transitive property, it can be inferred that the deformation on the surface was higher than that in the subsurface. This statement is only valid at the evaluated depth because, as described by Hertz's contact theory [53], other models [10,54,64] deformations is higher beneath the surface.

$$\alpha'_{(\%)_{sample1}} = 17.4424 + 0.7226x - 11.6940\ln x \quad (8)$$

$$\alpha'_{(\%)_{sample2}} = 48.6206 - 3.2284x - 4.4525\ln x \quad (9)$$

3.4. Influence of the burnishing parameters on the formation of α'-martensite in the surface layer

Fig. 13 shows the influence of the burnishing speed ($V_b = 10^2$, 10^3 and 10^4 mm/min), number of passes ($n = 1$, 3 and 5) and pressure (P = 16, 24, 32 and 40 MPa) on the strain-induced martensitic formation in the surface layer. In order to investigate the influence of the burnishing process on the burnished surface layer and establish a correlation with martensite formation, a random sample of microhardness profiles was chosen. The influence of the burnishing speed on the microhardness is shown in Fig. 14a and b, the influence of the number of passes is shown in Figs. 14c and d and the pressure is shown in Fig. 14e and f.

3.4.1. Influence of the burnishing speed

The GIXRD results presented in Fig. 10 showed that in addition, the formation of α'-martensite through LPB, its content is high on the surface. Both the fraction and the depth at which α'-martensite is formed strongly depend on the burnishing parameters. In general, the burnishing speed has a negligible influence on the fraction of α'-martensite formed with one burnishing pass, as seen in Fig. 13 ($n = 1$). In this case, the α'-martensite fraction reduces from 20 % at the surface and stabilizes in 3 % at a depth of 1 µm. This is due to the low degree of plastic strain, exception made for burnishing with a pressure of 40 MPa ($n = 1$), which showed the lowest martensite fraction for a speed of 10^4 mm/min (approximately 30 %), against approximately 80 % for burnishing speeds of 10^2 and 10^3 mm/min.

In contrast, under more severe plastic deformation conditions, for instance, increasing the number of passes or pressure, the influence of

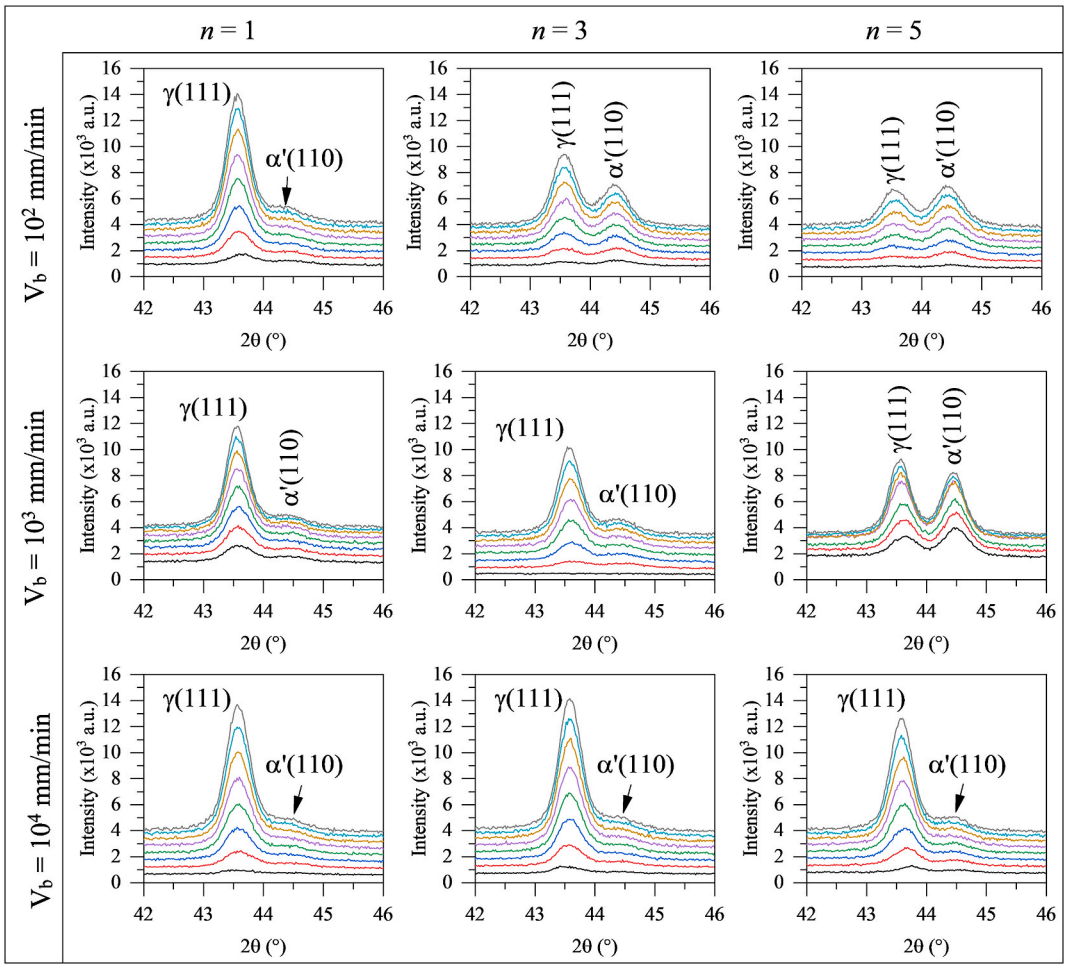

Fig. 10. GIXRD patterns at different grazing incidence angles for samples burnished at 16 MPa and distinct speeds and number of passes.

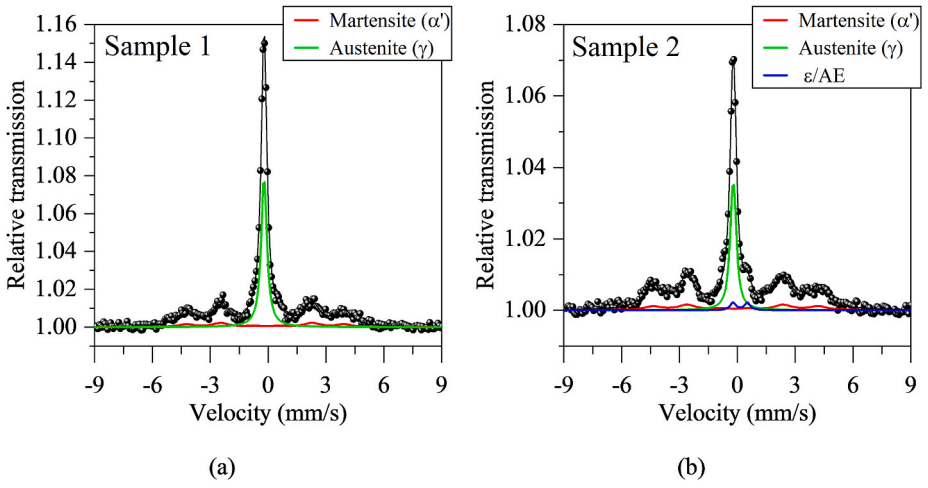

Fig. 11. Mössbauer spectra (CEMS) for burnished samples with: (a) P = 32 MPa, $V_b = 10^3$ mm/min and $n = 1$ and (b) P = 40 MPa, $V_b = 10^4$ mm/min and $n = 5$.

burnishing speed on α'-martensite formation is highlighted, as shown in Fig. 13 for $n = 3$ and $n = 5$. Under these conditions, increasing the burnishing speed decreases the fraction of α'-martensite. The depth is also affected, for instance, when burnishing is performed with a pressure of 24 MPa, speed of 10^4 mm/min and $n = 3$. Here, the fraction of α'-martensite begins to stabilize at approximately 1.5 μm below the surface, while at speeds of 10^2 and 10^3 mm/min, stabilization occurs below 2 μm. However, it should be emphasized that, although the α'-martensite content decreases with increasing velocity, the increase in the number of passes and pressure (parameters responsible for material hardening) increases the α'-martensite content even at high speeds. This phenomenon exhibited a resemblance to the outcomes observed by Sunil and Kapoor [65] in their compression tests of AISI 304L stainless Steel.

The microhardness results for the specimens burnished under a

Table 4
Hyperfine parameters at room temperature for samples 1 and 2.

Sample	Phase	$\delta \pm 0.05$ (mm/s)	$2\epsilon/\Delta Q \pm 0.05$ (mm/s)	$B_{hf} \pm 0.5$ (Tesla)	Content (%)
Sample1	Martensite (α')	−0.01	−0.06	25.40	45
	Austenite (γ)	−0.12	0.10	–	55
Sample2	Martensite (α')	−0.01	−0.02	26.59	59
	Austenite (γ)	−0.10	0.10	–	37

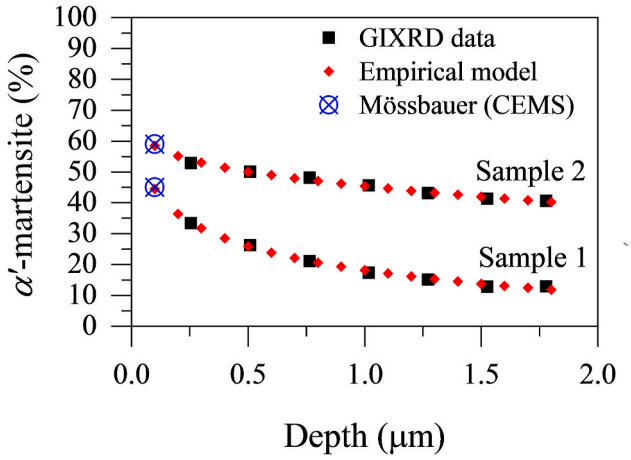

Fig. 12. Validation of the empirical model of the behavior of α'-martensite content as a function of depth based on GIXRD and Mössbauer spectra (CEMS).

pressure of 16 MPa, presented in Fig. 14a and b, show the influence of the burnishing speed on the surface layer (shallower than 2 μm). It can be noted that the surface hardness increases considerably, for all parameters tested, in comparison with the non-burnishing (NB) surface, confirming the occurrence of plastic deformation near the burnished surface. Similar to the GIXRD analyses (Fig. 13), that showed a low fraction of α'-martensite and negligible variation on α'-martensite fraction when the burnishing speed was increased for one pass, the microhardness results did not present an appreciable alteration when the burnishing speed increased from 10^2 to 10^3 mm/min, followed by a slight decrease when the burnishing speed was elevated to 10^4 mm/min (Fig. 14a). With the increase in the number of burnishing passes (Fig. 14b), the variation in microhardness between the speeds of 10^2 and 10^4 mm/min was wider, indicating a decrease in hardness with increasing speed. This behavior may be due to a possible decrease in the fraction of α'-martensite. At high speeds, the contact time between the tool and the work surface is shorter and possibly diminishes the deformation mechanisms over deeper layers. The burnishing speeds tested (10^2, 10^3 e 10^4 mm/min) produced a strain rate variation with one order of magnitude, thus affecting the deformation mechanisms significantly. At the highest strain rate, the reaction of the material to the hydrodynamic pressure imposed by the tool tends to restrict plastic deformation to regions closer to the surface, with lower intensity and depth. Since the driving force for strain-induced martensitic formation in LPB is plastic strain, the fraction of α'-martensite decreases, as well as the microhardness value. In addition to the metallurgical effects caused by the high strain rate, one must consider possible process instability due to tribological changes in contact between the ball and the workpiece, such as the stick-slip effect. Changes in the burnishing speed did not affect the surface microhardness after five burnishing passes. This result diverges from the transformed fraction of α'-martensite, which decreased with the elevation of burnishing speed. The microhardness test does not differentiate the possible phenomena involving plastic deformation, such as dislocations, deformation bands, martensite formation or twinning. It is known that increasing the strain rate also affects the thermodynamic phenomena related to strain-induced martensitic formation and this will be discussed later. Nevertheless, a tendency towards strain hardening saturation with the increase of the number of burnishing passes is observed. The reduction of the height of the deformation wave with the elevation of the number of passes (Fig. 7b) suggest strain hardening saturation.

3.4.2. Influence of the number of burnishing passes

Elevating the number of passes increases both the fraction of α'-martensite and the depth of the affected layer. The major difference is related to the fraction of α'-martensite formed. The number of burnishing passes plays a key role in the phase transformation induced by plastic deformation. The average fraction of α'-martensite is approximately 20 % when burnishing with one pass, while with five passes this value reaches 70 %. It is worth noting that the numerical simulation results indicated that the equivalent total strain almost doubled when the number of passes increased from one to three (see Fig. 6b). This increase in strain with increasing number of passes promotes additional work hardening of the burnished layer, generating more nucleation sites for the formation of α'-martensite and, consequently, reducing the energy required for the formation of the new phase during the subsequent pass. Another important aspect is the tendency to a reduction in the burnishing force when the number of burnishing passes is elevated (Fig. 7b), which is a direct consequence of strain hardening saturation with an increasing number of passes (identified by the reduction in the height of the deformation wave). This behavior suggests that the process tends to substantially affect near surface layers and explains the higher fraction of α'-martensite formed on the surface. For lower burnishing pressures (16 and 24 MPa) associated with the highest burnishing speed (10^4 mm/min) there is a tendency to reduce the fraction of α'-martensite, even with threes or five passes (see Fig. 13). This may indicate a concurrence of plastic deformation and thermodynamic mechanisms associated with strain-induced martensitic formation.

The surface microhardness results point to the same trend as the GIXRD analysis (Fig. 13, confirming the effect of increased strain hardening on the burnished surface with the elevation of the number of passes (see Fig. 14c and d). This effect is less evident when burnishing at high speeds, as can be seen in Fig. 14d, where the surface microhardness variation is not as evident as the phase transformation. As previously mentioned, it is not possible to distinguish the effect of strain hardening, deformation bands, twinning and α'-martensite formation in this test. An aspect worth mentioning is the highest microhardness value close to the surface and its saturation at a depth of 1.5 μm, indicating the tendency to form a nanostructured layer [36].

3.4.3. Influence of the burnishing pressure

Not surprisingly, increasing the burnishing pressure (mechanical driving force) elevated the fraction of α'-martensite induced by plastic strain, additionally to keeping this fraction more stable at a deeper distance from the surface and forming a more homogeneous layer. In contrast, it is difficult to dissociate the influence of pressure with speed and the number of burnishing passes, since each burnishing condition is governed by a parameter, e.g., with one burnishing pass and speed of 10^2 mm/min, the fraction of α'-martensite increases with increasing pressure. In this case, burnishing pressure governs the formation of α'-martensite, see Fig. 13. When the burnishing speed increases to 10^4 mm/min, no significant variation on the α'-martensite fraction is observed, condition governed by the burnishing speed. When the number of burnishing passes is increased, burnishing pressure becomes a relevant parameter due to the continuous deformation promoted by the increased number of passes, which form nucleation sites, thus reducing the energy required for α'-martensite formation. In this scenario, number of passes becomes more critical and intensifies the effects promoted by the increased burnishing pressure. The fraction of α'-martensite was lower when a pressure of 24 MPa was applied for the samples burnished

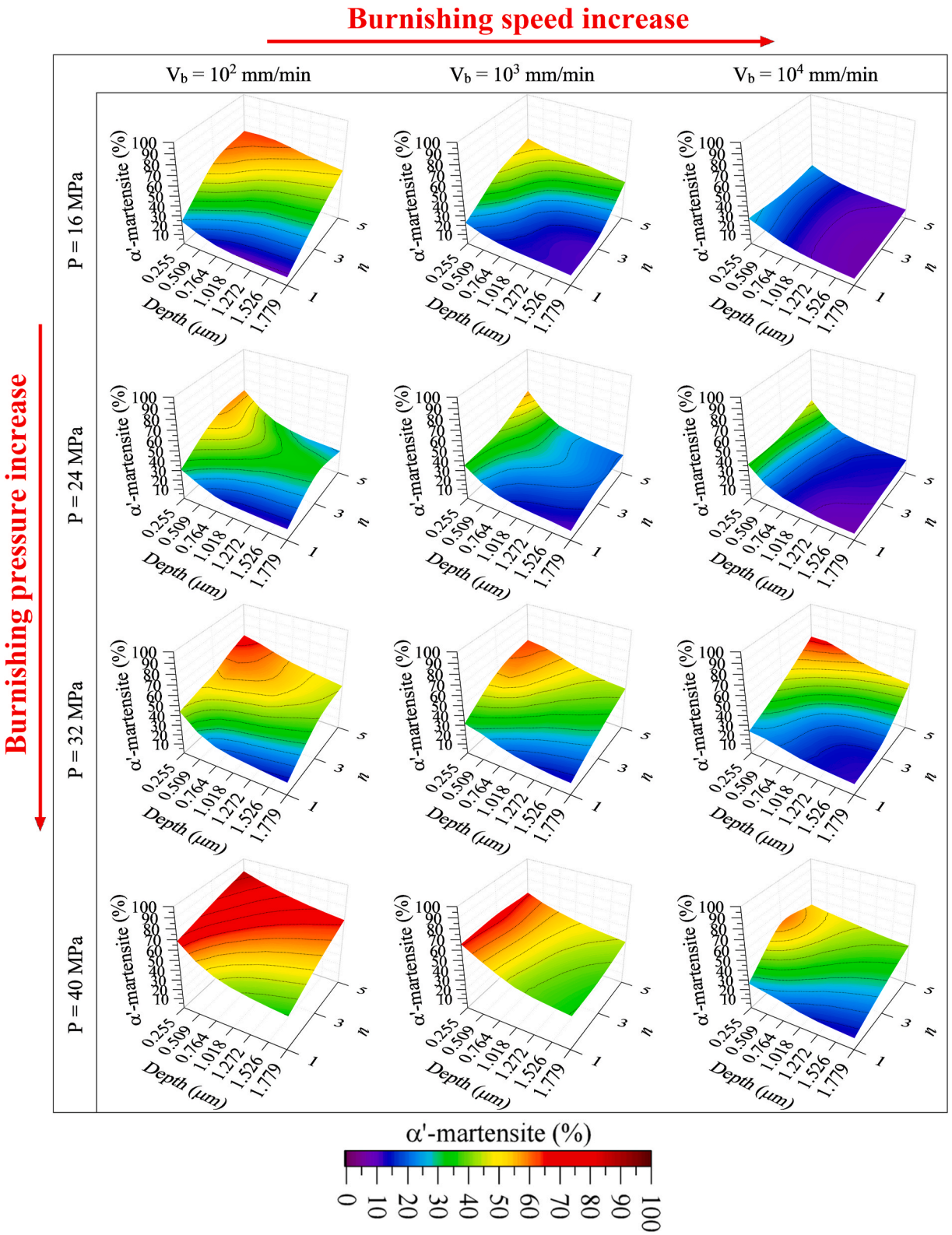

Fig. 13. Influence of the burnishing speed, number of passes and pressure on α'-martensitic formation in the surface layer.

with $n = 5$ and $V_b = 10^2$ and 10^3 mm/min, as can be seen in Fig. 13. Contact between the ball and the cage took place during the process and possibly influenced the result.

The microhardness values were not drastically affected when burnishing pressure was altered for a speed of 10^2 mm/min and, in general, an increase in hardness is observed with the elevation of burnishing pressure. Again, the possible contact between the ball and the cage possibly affected the deformation process, resulting in the lowest hardness for a burnishing pressure of 24 MPa (see Fig. 14e). Increasing the burnishing speed from 10^2 to 10^3 mm/min resulted in a slight decrease in the microhardness values obtained fora pressure of 40 MPa and the highest hardness is recorded for a pressure of 32 MPa (see

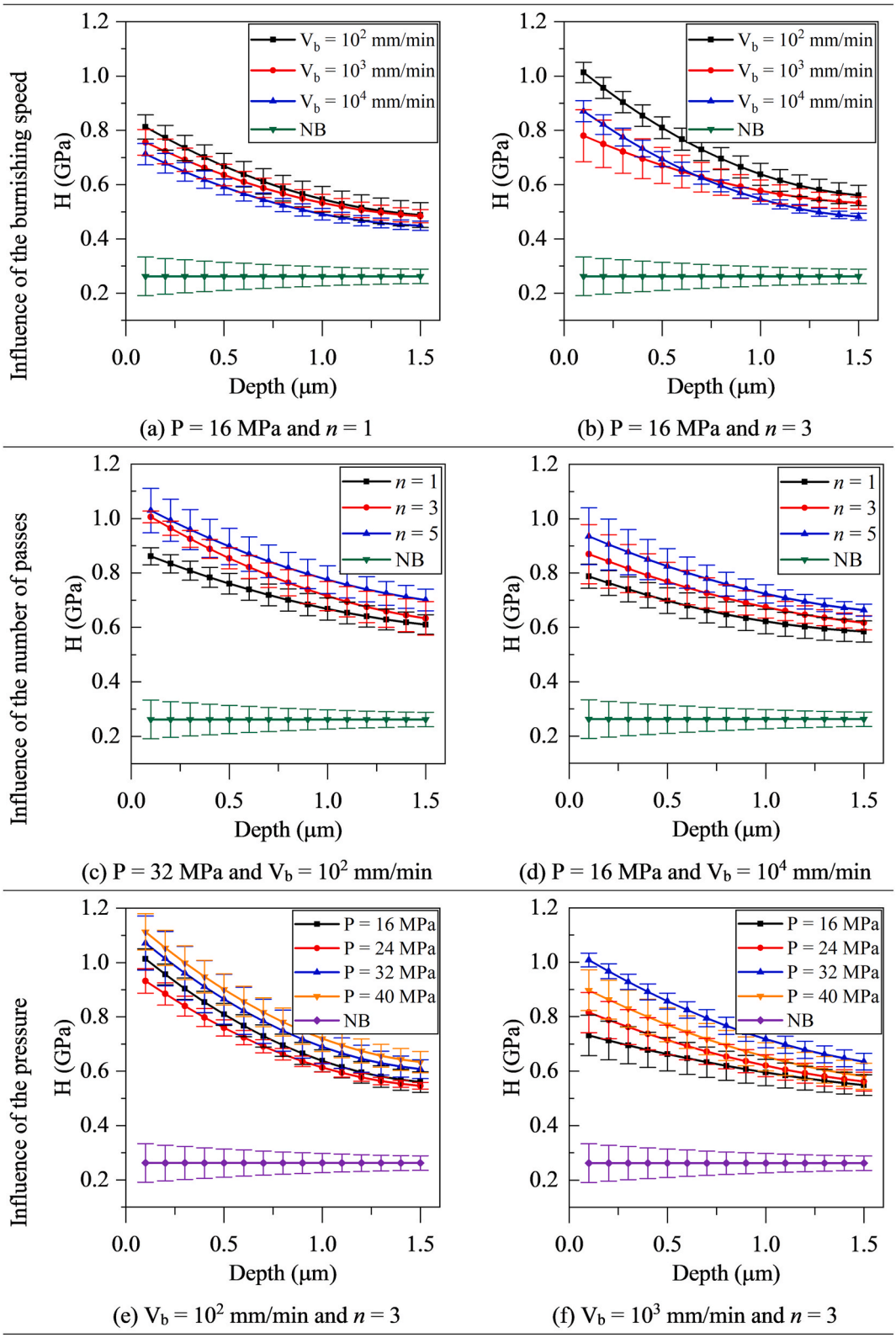

Fig. 14. Influence of the burnishing speed, number of passes and pressure on α'-martensitic formation in the surface layer.

Fig. 14f). It is worth mentioning that the pressure of 32 MPa promoted the highest burnishing force and some samples presented surface damage when burnished with 40 MPa. Moreover, the variation in microhardness increased when pressure was elevated. This effect is analogous to that observed in the previously mentioned analysis of the α'-martensite formation.

3.4.4. *Comprehensive analysis of strain-induced martensitic formation during LPB*

This analysis aims to present, with a confidence level of 95 %, the effect of the main burnishing parameters on strain-induced α'-martensite formation (Fig. 15) and the possible interactions between them. All the analyzed parameters presented a statistically significant influence on the

formation of α'-martensite. The number of passes presented the highest statistical contribution (30.11 %), followed by pressure (28.04 %) and burnishing speed (18.14 %).

Increasing the burnishing speed reduces the fraction of α'-martensite (Fig. 15a). In addition to the tribological effect that may have generated instability in the contact between the ball and the part, the metallurgical effect due to the increased strain rate was probably the most influential factor in the strain-induced phase transformation. The influence of increasing the strain rate in austenitic stainless steels is rather complex and involves more than dislocation gliding and twinning. According to Xia et al. [66], the formation of α'-martensite from metastable austenite is exothermal and the dissipation of the heat generated in the process from the external plastic work together with the internally generated latent heat changes the thermodynamic state from isothermal to adiabatic, which modifies the deformation mechanisms, reducing or inhibiting the formation of α'-martensite, also reported by Krupp [67]. The decrease in α'-martensite content due to the adiabatic heating effect can be explained by the localized temperature increase. This temperature rise leads to an increase in Stacking Fault Energy (SFE). As a result, the decrease in stacking fault width, making the processes of nucleation and subsequent growth of α'-martensite more difficult. Thus, the transformation of γ-austenite into α'-martensite is suppressed [65]. Further studies concerned with the influence of strain rate on the burnishing temperature in AISI 304 shall be conducted in order to better elucidate this phenomenon. Martins et al. [68] found that the highest temperature developed in LPB of hardened AISI 4140 steel was recorded on the surface (80 °C). It should be pointed out that due to its microstructure, the deformation of AISI 304 stainless steel is more severe than that of hardened AISI 4140 steel, therefore, it is likely that the temperature reached when burnishing the AISI 304 steel is higher than 80 °C. Additionally, the effect caused by the decreased contact time between the ball and the work material reduces the response time to the stress imposed by the burnishing tool. Consequently, LPB carried out at high speeds tends to affect a layer closer to the surface. The microhardness tests also show this effect, see Fig. 14.

Fig. 15b shows that increasing the number of burnishing passes elevates the fraction of α'-martensite due to additional surface strain hardening (shown in the numerical simulation results presented in Fig. 6b and microhardness results in Fig. 14c and d). The slope of the curve between one and three burnishing passes is much steeper than from three to five passes. This behavior indicates that the strain hardening tends to saturate in the final passes, as observed by the variation in the fraction of α'-martensite (approximately 7 % between three and five passes versus 17 % between one and three passes). This result is further corroborated by the strain wave profilometry analysis presented in Fig. 7, which showed a decrease in the height of the deformation wave

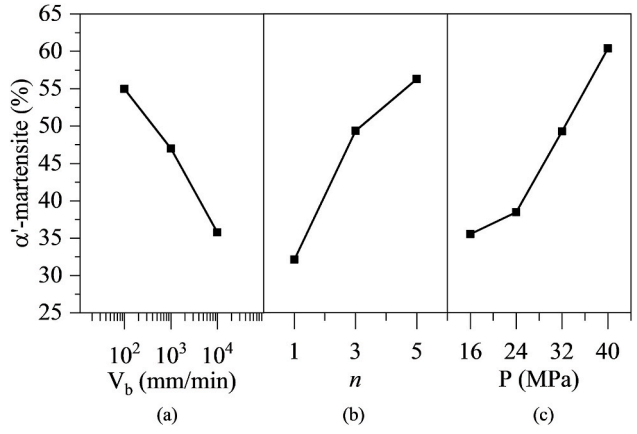

Fig. 15. Main effect plots for α'-martensite formation: (a) speed, (b) number of passes and (c) pressure.

with an increasing number of passes. Fig. 16a presents the EBSD inverse pole figure (IPF) maps of the sample burnished with one pass (P = 24 MPa and $V_b = 10^3$ mm/min). It is observed that a single burnishing pass is not able to significantly change the microstructure of the material, as suggested by the band contrast maps presented in Fig. 16b. This map indicates a higher percentage (89.4 %) of high angle contours (> 15°) against 6.7 % of low angle contours (2°–5°), which correspond to the most concentrated dislocations at the grain boundaries. The additional deformation achieved by increasing the number of passes produces a refined grain layer on the burnished surface, as can be seen in the IPF map of Fig. 16c. Sohrabi et al. [69] demonstrated a significant influence of grain size on α'-martensite formation. In general, an increase in grain size up to the transition range of 34–90 μm (the measured average grain size of the material used in this study was 80 μm) reduces the stacking fault energy and consequently promotes α'-martensitic transformation. In this case, the decrease in the α'-martensite content observed between three and five passes (reduction in the slope of the curve shown in Fig. 15b), in addition to the reduced deformation, may also be attributed to the grain size reduction. A high concentration of high angle contours near the surface is observed together with a considerably higher amount (72.1 %) of low angle contours (Fig. 16d), which correspond, in addition to dislocations, mainly to deformation bands concentrated in the interior of the grains and extending to the deeper burnished layers, indicating that the severity of the deformation process increased with this parameter. Subsequent deformation passes produce more deformation bands, which are preferred sites for nucleation of α'-martensite, reducing the energy required for the formation of the new phase, and explains both the elevated fraction and its higher contribution to α'-martensite formation.

The increase in burnishing pressure (Fig. 15c) also elevates the fraction of α'-martensite. Under low pressures (16 and 24 MPa), this variation is not relevant (less than 5 %), being more evident (approximately 25 %) when LPB is performed under higher pressures. Increasing burnishing pressure elevates the intensity of plastic deformation, as seen in Fig. 6c, consequently increasing the driving force for phase transformation. However, an excessively high burnishing pressure can cause a damage to the workpiece surface, leading to early failure or unsuitability of the burnished product, see Fig. 8d.

Regarding the interactions, only the interaction speed-number of passes was not significant. The pressure-speed (Fig. 17a) and pressure-number of pass (Fig. 17b) interactions presented contributions of 3.5 and 3.16 %, respectively. The reduction of burnishing speed associated with the increase of pressure promoted an increase in the fraction of the α'-martensite. In terms of mechanisms, it can be inferred that the increase in pressure (stronger driving force) associated with the reduction in burnishing speed (longer contact time between the ball and the work material) provided an adequate response time of the work material to the plastic deformation mechanisms and favored conditions to both the formation of strain-induced α'-martensite and the increase of its fraction and depth of the affected layer.

Increasing the number of passes associated with elevating the burnishing pressure induces the formation of α'-martensite and the increase of its fraction and depth of the affected layer. Both parameters are sources of driving force for the strain-induced phase transformation. Increasing the number of burnishing passes promotes additional deformation during each pass, continuously strain hardening the material and forming sites for nucleation of α'-martensite, while increasing the burnishing pressure raises the intensity of the driving force. Considering that strain hardening is limited, the strain tends to saturate. This phenomenon can be observed when pressure is increased from 32 to 40 MPa with five burnishing passes (Fig. 17b). Although there is no interaction between speed and the number of burnishing passes, the results indicated an interaction between the three factors, with a contribution of 8.58 %. Therefore, the analysis must encompass the effect of the interaction between speed and number of passes (Fig. 17c). At the lower

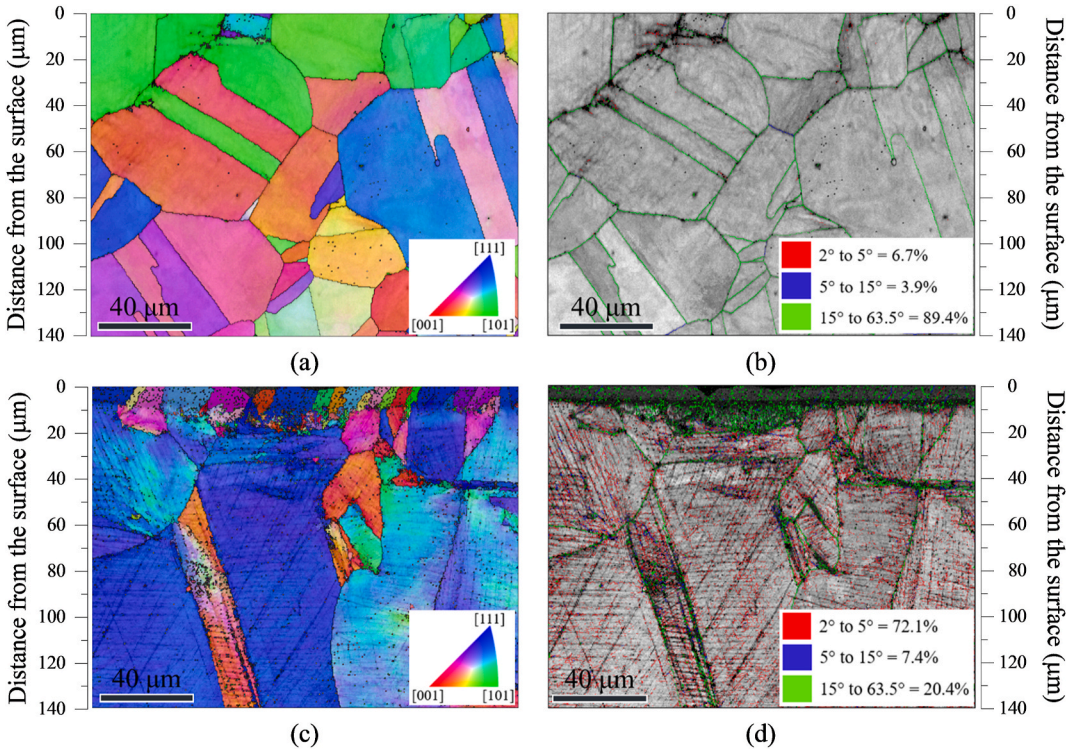

Fig. 16. EBSD results: (a) IFP and (b) band contrast maps of the sample burnished with one pass; and (c) IFP and (d) band contrast maps of the sample burnished with five passes.

burnishing speed (10^2 mm/min), a larger amount of α'-martensite is formed when the number of passes and pressure increase. In this case, one must consider that the lower burnishing speed leads to a lower temperature (absence of the adiabatic effect). Furthermore, the contact time during which the workpiece will be subject to the stress imposed by the burnishing tool increases, in addition to more sites for α'-martensite nucleation during each burnishing pass without strain hardening saturation. At intermediate and high burnishing speeds, no variation in the tendency to form α'-martensite is observed when the number of passes is elevated.

3.5. Correlation between α'-martensite formation and surface topography

Fig. 18 presents the influence of the burnishing parameters assessed in terms of the continuous wavelet transform (CWT) and correlates a morphological roughness scale to the wavelengths of continuous wavelets. The relationship between frequency and space is characterized by the location of the structure at different scales [70]. The indications of local extremes for longer wavelengths are presented on higher scales and, for short wavelengths, on lower scales.

LPB is commonly applied after machining operations. The machining parameters influence the roughness and the initial roughness condition can affect the results obtained after LPB. In order that initial roughness would not be a significant input parameter in the phase transformation analyses and in the correlation between phase transformation and roughness of the burnished surface, the tests were performed on polished samples. The results show that the waviness surface has amplitudes of the nanometer order, with an average Wa value of 19.48 nm.

For all burnishing parameters tested, the waviness was higher compared to that of the polished sample. This occurs due to the plastic flow of material from the deformation process induced by the LPB. The strain intensity, and consequently the waviness response, will be affected by the LPB parameters. It can be seen that burnishing speed (Fig. 18a), at both the lowest ($V_b = 10^2$ mm/min) and highest levels ($V_b = 10^4$ mm/min), tends to affect the roughness profile at macrogeometric scales (wavelength of 1 mm). The numerical simulation showed that the equivalent total strain at speed of 10^4 mm/min is slightly lower than at speed of 10^2 mm/min. However, due to the lower friction between the ball and the workpiece at the highest speed, the surface strains tended to be more homogeneous, which contributed to the wave formation, as seen in Fig. 6a. It is likely that homogenization of the strains on the surface has affected the waviness profile, even though the fraction α'-martensite has been reduced at highest speed. Additional burnishing passes increased waviness profile (Fig. 18b). Obviously, this result is a consequence of the increase in plastic strain caused by the increase in this parameter, as indicated by the numerical simulation (Fig. 6b). With one burnishing pass, deformation is concentrated on micrometric roughness scales, with a wavelength of 0.2 mm (value that corresponds to twice the step-over of 0.1 mm). Therefore, only the roughness peaks are deformed, filling in the roughness valleys, which indicates a low intensity of surface plastic deformation, reason why the fraction of α'-martensite formed is lower. When the number of passes is increased, deformation becomes more intense and reaches macroscopic roughness scales. With five passes, deformation is severe enough to break the periodicity of the microgeometric roughness profiles, affects the macroscopic scale to values that exceed a wavelength of 1 mm and produces roughness scales with a wavelength lower than 0.2 mm. In this case, the flow and amplitude of displaced material is considerably higher, thus explaining the higher fraction of α'-martensite formed. The number of burnishing passes presented the highest influence on both the fraction and depth of α'-martensite formed and on the roughness profiles at microgeometric and macrogeometric scales. Increasing the burnishing pressure (Fig. 12c) produces a similar effect to the number of passes: it is expected that increasing pressure raises the hydrostatic driving force and elevates the strain state of the surface. As a consequence, it raises the fraction of α'-martensite.

Since deformation in LPB tends to affect the roughness on a macrogeometric scale, it becomes relevant to evaluate the waviness amplitude parameters. To statistically evaluate the effect of deformation on the surfaces and, consequently, on the formation of α'-martensite, the

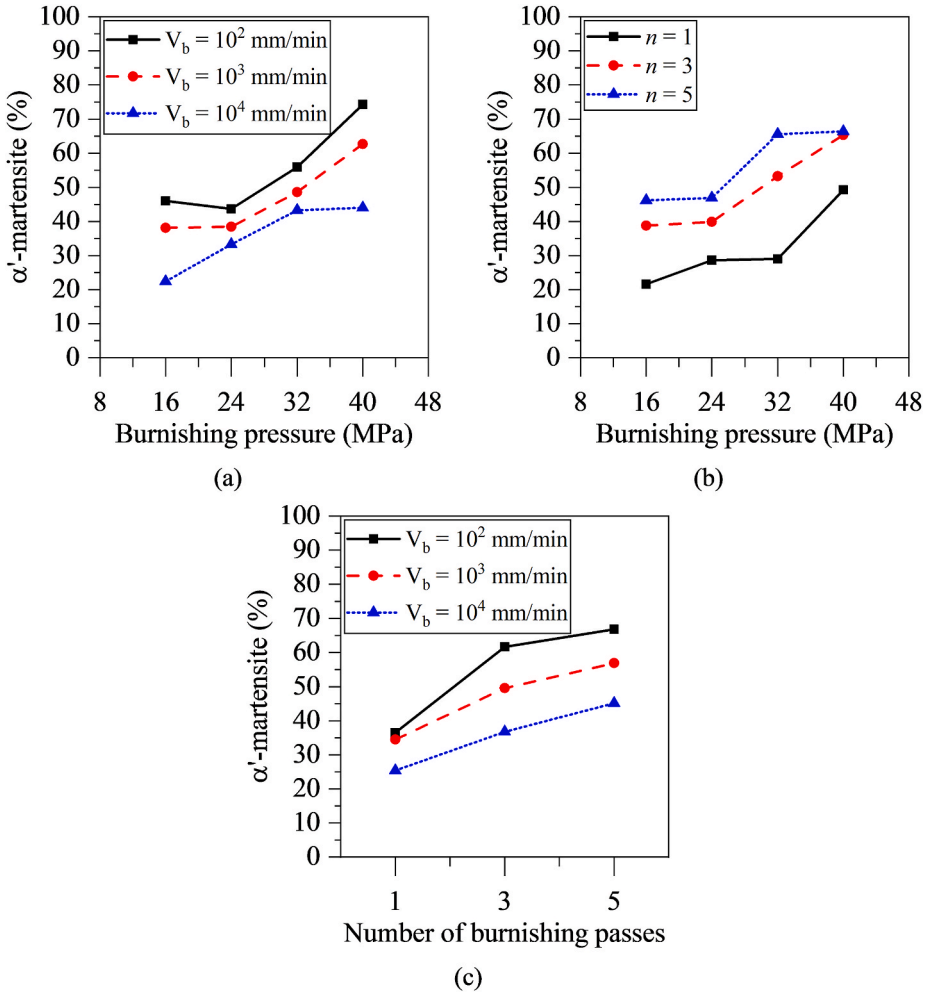

Fig. 17. Interaction plots for α'-martensite formation: (a) pressure-speed (b) pressure-number of passes.

arithmetic mean waviness (Wa) parameter was used. The main effects of LPB parameters on Wa are shown in Fig. 19 (left) together with the waviness surfaces (right), which qualitatively present the effect of LPB parameters on surface deformation.

There was no statistical difference in the Wa values between burnishing speeds of 10^2 and 10^4 mm/min (Fig. 19a). This result is relevant, because it indicates that even at high speed, plastic deformation on the surface was severe and the reduction in the fraction of α'-martensite is a consequence of changing strain-related phenomena, particularly due to the adiabatic effect. Undoubtedly, the mechanical and metallurgical responses of the high speed burnishing operation are very complex, as it involves changes in tribological behavior, which alters the contact conditions and causes process instability, and microstructural change, which is a result of thermodynamic effects caused by the increased strain rate. The numerical model identified lower equivalent total strains on the surface for the speed of 10^4 mm/min speed, but the order of magnitude was close to that presented for the 10^2 mm/min speed. Thus, the strain values in the high speed model may be associated with a contact nonlinearity problem, as well as the behavior of the material subjected to high strain rates. In addition to the reduction in friction, which contributed to the homogenization of surface strains at the highest speed, there was also a reduction in surface microhardness due to the higher austenitic content, whose mechanical strength is lower than that of α'martensite. Thus, the flow of material may have been favored, which contributed to the Wa values at speed 10^4 mm/min being similar to those at speed 10^2 mm/min. Except for burnishing speed, the Wa curves as functions of increasing number of passes and pressure show a similar behavior to the α'-martensite fraction curves, i.e., elevating these parameters increases both the fraction of α'-martensite and Wa. The influence of number of passes (Fig. 19b) is more evident when compared to the other parameters: the value of Wa doubled when the number of passes increased and this effect is demonstrated by the waviness surface. For a single burnishing pass, the waviness is barely affected and the wave amplitudes are short because the strain is low. Increasing the number of passes promotes additional localized deformation (see Fig. 6b), repeatedly in the same region, which makes the deformation state more severe, raising the plastic flow. Thus, both the amplitude and the wavelength increase. This result demonstrates the tendency of the increased number of passes to affect with higher intensity and depth beneath the surface and, consequently, to form a larger fraction of α'-martensite and at a deeper layer. Increasing burnishing pressure increases the wave amplitude due to increased hydrostatic force (Fig. 19c), however, its effect is less pronounced than the number of passes.

A correlation between Wa and both the height caused by grain deformation (H) and the degree of fatigue damage under low-cycle fatigue (UF) on austenitic stainless steel was investigated [71]. The results shown that Wa increased when H or UF are elevated and these parameters are strongly correlated and affected by deformation. These results demonstrate an embrittlement of the material as a function of these parameters. In contrast, Wa increases with increasing α'-martensite fraction. This result may considerably mitigate the embrittlement effect due to the increased flow stress and the higher compressive residual stresses induced in the α'-martensite.

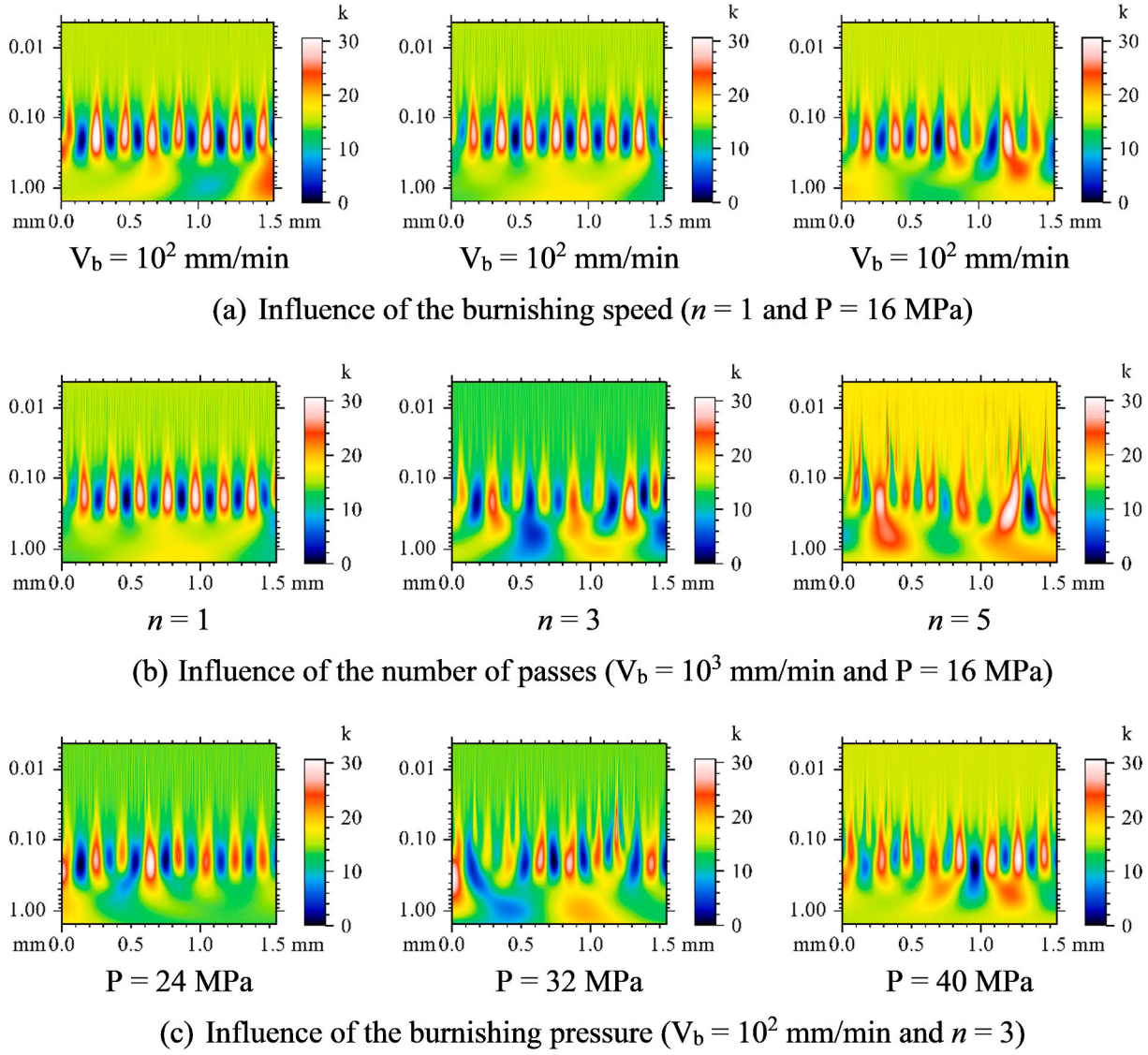

Fig. 18. Continuous wavelet transform analysis: influence of (a) burnishing speed, (b) number of passes and (c) pressure.

4. Conclusions

After subjecting AISI 304 austenitic stainless steel to low plasticity burnishing under various conditions, the following conclusions can be drawn.

- Concerning the numerical simulation results, higher LPB speed reduced friction, leading to decreased and more uniform strain. Conversely, increasing the number of passes and pressure increased the strain intensity and plastically deformed area.
- Regarding the burnishing LPB force, increasing LPB speed reduced the burnishing force owing to the reduction in the contact time between ball and material surface, potentially reducing plastic deformation. Increasing the number of passes reduces LPB force due to decreased contact area between the ball and the workpiece, a result of material work hardening. An increase in pressure elevates the LPB force up to a maximum value, after which it decreases and becomes detrimental to the surface.
- With regard to α'-martensite formation, empirical model (GIXRD analysis ranging from 0.255 to 2 μm in depth), corroborated by Mössbauer spectroscopy analysis (depth of ≈0.1 μm) revealed that the highest α'-martensite content occurs at the surface and decreases with depth. Such behavior diverges from the predictive models. The number of LPB passes played the most significant role in martensite α'-formation and its increase resulted in higher α'-martensite layer content and depth, along with high microhardness values and the formation of a refined grain surface layer. Raising LPB speed reduced α'-martensite content, depth, and microhardness due to the adiabatic effect. Increasing the LPB pressure elevated the fraction of α'-martensite formed.
- Concerning the correlation between α'-martensite and the arithmetic mean waviness, increasing the number of LPB passes led to an increase in the amplitude of the waviness, indicating higher severity of plastic deformation on the surface, similarly to the formation of α'-martensite. Increasing pressure elevates wave amplitude due to increased hydrostatic force and, analogous to the α'-martensitic phase transformation, this effect was less pronounced in comparison with number of passes.

The authors are grateful to the Mechanical Engineering Graduate Program of the Catholic University of Minas Gerais and University de Minas Gerais and the Brazilian research agencies CAPES (project: 88887.692433-2022-00), CNPq and FAPEMIG for financial support.

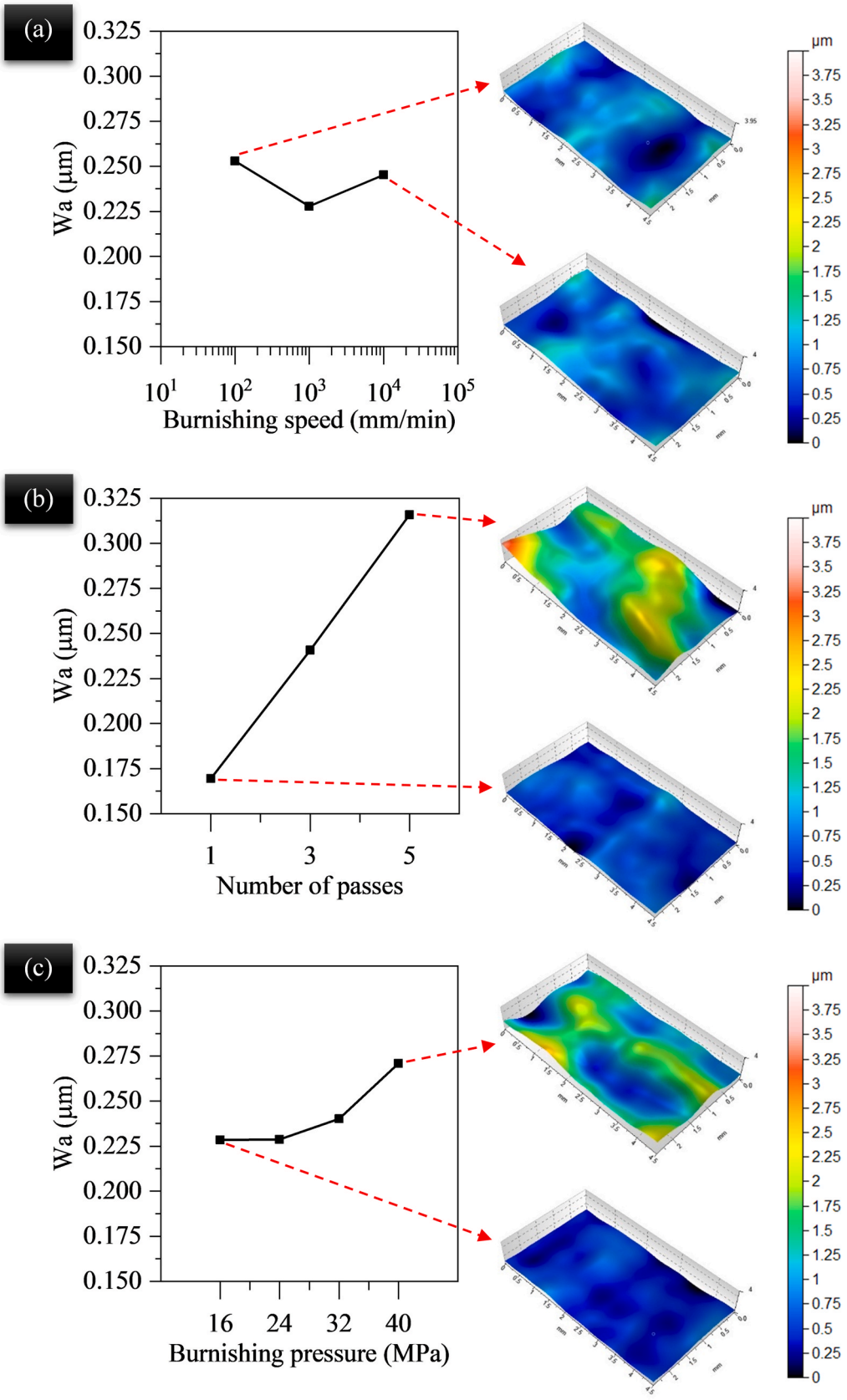

Fig. 19. Influence of (a) burnishing speed, (b) number of passes and (c) pressure on the arithmetic mean waviness (Wa) and waviness surfaces.

Declarations

Funding

This study was partly financed in part by the Coordenação de Aperfeiçoamento de Pessoal de Nível Superior - Brasil (CAPES) - Finance Code 001.

Ethics approval

Not applicable.

Consent to participate

All the authors consent to participate in this research.

Consent for publication

The authors give full consent to the publisher for the publication of this work.

Availability of data and materials

Not applicable.

Code availability

Not applicable.

Declaration of competing interest

The authors declare that they have no known competing financial interests or personal relationships that could have appeared to influence the work reported in this paper.

References

[1] Schulze V. Modern mechanical surface treatment. Weinheim, Alemanha: WILEY-VCH Verlag GmbH & Co. KGaA; 2004. https://doi.org/10.1002/3527607811.
[2] Abrão AM, Denkena B, Breidenstein B, Mörke T. Surface and subsurface alterations induced by deep rolling of hardened AISI 1060 steel. J Inst Eng Prod 2014;8(5):551–8. https://doi.org/10.1007/s11740-014-0539-x.
[3] Delgado P, Cuesta I, Alegre J, Díaz A. State of the art of deep rolling. Precis Eng 2016;46:1–10. https://doi.org/10.1016/j.precisioneng.2016.05.001.
[4] Hua Y, Liu Z, Yi J, Tang A. Studies on the microstructural evolution and mechanical properties of superalloy inconel 718 induced by low plasticity burnishing coupled with turning. Materials 2022;15(11). https://doi.org/10.3390/ma15113740.
[5] Zhang T, Bugtai N, Marinescu ID. Burnishing of aerospace alloy: a theoretical–experimental approach. J Manuf Syst 2015;37:472–8. https://doi.org/10.1016/j.jmsy.2014.11.004.
[6] Hornbach DJ, Prevey PS, Loftus EF. Application of Low Plasticity Burnishing (LPB) to improve the fatigue performance of Ti-6AI-4V femoral hip stems. J ASTM Int (JAI) 2006;3(5). https://doi.org/10.1520/jai13580.
[7] Thesleff A, Ortiz-Catalan M, Brånemark R. Low plasticity burnishing improves fretting fatigue resistance in bone-anchored implants for amputation prostheses. Med Eng Phys 2022;100:103755. https://doi.org/10.1016/j.medengphy.2022.103755.
[8] Scheel JE, Hornbach DJ, Prevey PS. Mitigation of stress corrosion cracking in nuclear weldments using low plasticity burnishing, International Conference on Nuclear Engineering. Proceedings, ICONE 2008;1(January 2008):649–56. https://doi.org/10.1115/ICONE16-48597.
[9] Anirudh PV, Kumar B, Girish G, Shailesh S, Oyyaravelu R, Kannan C, et al. Effect of cryogenics-assisted low-plasticity burnishing on laser-clad stellite 6 over SS420 substrate. J Mater Eng Perform 2020;29(10):6861–9. https://doi.org/10.1007/s11665-020-05152-7.
[10] Magalhães FC, Abrão AM, Denkena B, Breidenstein B, Mörke T. Analytical modeling of surface roughness, hardness and residual stress induced by deep rolling. J Mater Eng Perform 2017;26(2):876–84. https://doi.org/10.1007/s11665-016-2486-5.
[11] Schuh A, Zeller C, Holzwarth U, Kachler W, Wilcke G, Zeiler G, et al. Deep rolling of titanium rods for application in modular total hip arthroplasty. J Biomed Mater Res B Appl Biomater 2007;81B(2):330–5. https://doi.org/10.1002/jbm.b.30669.
[12] Kloos K, Fuchsbauer B, Adelmann J. Fatigue properties of specimens similar to components deep rolled under optimized conditions. Int J Fatig 1987;9(1):35–42. https://doi.org/10.1016/0142-1123(87)90087-9.
[13] Gharbi K, Ben Moussa N, Ben Rhouma A, Ben Fredj N. Improvement of the corrosion behavior of AISI 304L stainless steel by deep rolling treatment under cryogenic cooling. Int J Adv Manuf Technol 2021;117(11–12):3841–57. https://doi.org/10.1007/s00170-021-07744-6.
[14] Gharbi K, Ben Moussa N, Fredj NB. Corrosion resistance enhancement of aisi 304 stainless steel by deep rolling treatment. In: Kharrat M, Baccar M, Dammak F, editors. Advances in mechanical engineering, materials and mechanics. Cham: Springer International Publishing; 2021. p. 233–9.
[15] ben Moussa N, Gharbi K, Chaieb I, Ben Fredj N. Improvement of AISI 304 austenitic stainless steel low-cycle fatigue life by initial and intermittent deep rolling. Int J Adv Manuf Technol 2018;101(1–4):435–49. https://doi.org/10.1007/s00170-018-2955-0.
[16] Chomienne V, Valiorgue F, Rech J, Verdu C. Influence of ball burnishing on residual stress profile of a 15-5ph stainless steel. CIRP J Manuf Sci Technol 2016;13:90–6. https://doi.org/10.1016/j.cirpj.2015.12.003.
[17] Rodríguez A, López de Lacalle L, Celaya A, Lamikiz A, Albizuri J. Surface improvement of shafts by the deep ball-burnishing technique. Surf Coating Technol 2012;206(11):2817–24. https://doi.org/10.1016/j.surfcoat.2011.11.045.
[18] Uddin MS, Hall C, Hooper R, Charrault E, Murphy P, Santos V. Finite element analysis of surface integrity in deep ball-burnishing of a biodegradable az31b mg alloy. Metals 2018;8(2). https://doi.org/10.3390/met8020136. URL, https://www.mdpi.com/2075-4701/8/2/136.
[19] Hassan AM, Al-Wahhab OMA. Surface characteristics of some roller burnished non-ferrous components. Mater Manuf Process 1998;13(4):505–15. https://doi.org/10.1080/10426919808935272.
[20] El-Khabeery M, El-Axir M. Experimental techniques for studying the effects of milling roller-burnishing parameters on surface integrity. Int J Mach Tool Manufact 2001;41(12):1705–19. https://doi.org/10.1016/S0890-6955(01)00036-0.
[21] Morimoto T. Work hardening and tool surface damage in burnishing. Wear 1988;127(2):149–59. https://doi.org/10.1016/0043-1648(88)90127-5.
[22] Hassan AM. The effects of ball- and roller-burnishing on the surface roughness and hardness of some non-ferrous metals. J Mater Process Technol 1997;72(3):385–91. https://doi.org/10.1016/S0924-0136(97)00199-4.
[23] Al-Qawabeha UF. The effect of diamond pressing and roller burnishing of unheat treated carbon steel surfaces. Mach Sci Technol 2007;11(1):145–55. https://doi.org/10.1080/10910340601172255.
[24] Cagan SC, Tasci U, Pruncu CI, Bostan B. Investigation of the effects of eco-friendly MQL system to improve the mechanical performance of WE43 magnesium alloys by the burnishing process. J Braz Soc Mech Sci Eng 2022;45(1):1–15. https://doi.org/10.1007/s40430-022-03925-w.
[25] Bhaduri A. Mechanical properties and working of metals and alloys, vol. 264. Springer Singapore; 2018. https://doi.org/10.1007/978-981-10-7209-3.
[26] Stout MG, Follansbee PS. Strain rate sensitivity, strain hardening, and yield behavior of 304L stainless steel. J Eng Materi Technol, Transactions of the ASME 1986;108(4):344–53. https://doi.org/10.1115/1.3225893.
[27] Muñoz-Cubillos J, Coronado J, Rodríguez S. Deep rolling effect on fatigue behavior of austenitic stainless steels. Int J Fatig 2017;95:120–31. https://doi.org/10.1016/j.ijfatigue.2016.10.008.
[28] Maximov J, Duncheva G, Anchev A, Dunchev V, Argirov Y. Effect of diamond burnishing on fatigue behaviour of aisi 304 chromium-nickel austenitic stainless steel. Materials 2022;15(14). https://doi.org/10.3390/ma15144768.
[29] Juijerm P, Altenberger I. Fatigue performance enhancement of steels using mechanical surface treatments. J Metal Mater Mine Apr. 2017;17(1).
[30] Kongthep J, Timmermann K, Scholtes B, Niendorf T. On the impact of deep rolling at different temperatures on the near surface microstructure and residual stress state of steel aisi 304. Mater Werkst 2019;50(7):788–95. https://doi.org/10.1002/mawe.201700198.
[31] Staudhammer K, Murr L, Hecker S. Nucleation and evolution of strain-induced martensitic (b.c.c.) embryos and substructure in stainless steel: a transmission electron microscope study. Acta Metall 1983;31(2):267–74. https://doi.org/10.1016/0001-6160(83)90103-7.
[32] Wang B, Hong C, Winther G, Christiansen TL, Somers MA. Deformation mechanisms in meta-stable and nitrogen-stabilized austenitic stainless steel during severe surface deformation. Materialia 2020;12:100751. https://doi.org/10.1016/j.mtla.2020.100751.
[33] Briant CL, Ritter AM. The effects of deformation induced martensite on the sensitization of austenitic stainless steels. Metall Trans A 2013;11A:2009–17. https://doi.org/10.1007/BF02655120.
[34] Eliezer D, Chakrapani DG, Altstetter CJ, Pugh EN. The influence of austenite stability on the hydrogen embrittlement and stress- corrosion cracking of stainless steel. Metall Trans A 1979;10(7):935–41. https://doi.org/10.1007/BF02658313.
[35] Spencer K, Embury J, Conlon K, Véron M, Bréchet Y. Strengthening via the formation of strain-induced martensite in stainless steels. Mater Sci Eng, A 2004;387–389:873–81. https://doi.org/10.1016/j.msea.2003.11.084. 13th International Conference on the Strength of Materials.
[36] Nikitin I, Altenberger I. Comparison of the fatigue behavior and residual stress stability of laser-shock peened and deep rolled austenitic stainless steel aisi 304 in the temperature range 25–600°c. Mater Sci Eng, A 2007;465(1):176–82. https://doi.org/10.1016/j.msea.2007.02.004.
[37] Dreano A, Alnajjar M, Salvatore F, Rech J, Bosch C, Wolski K, et al. Effect of ball-burnishing on hydrogen-assisted cracking of a martensitic stainless steel. Int J Hydrogen Energy 2022;47(93):39654–65. https://doi.org/10.1016/j.ijhydene.2022.09.110.

[38] Rodriguez T, Antonio J. Effects of a ball-burnishing process assisted by vibrations in g10380 steel specimens. Int J Adv Des Manuf Technol 2015;81:1757–65. https://doi.org/10.1007/s00170-015-7255-3.
[39] Loh N, Tam S. Effects of ball burnishing parameters on surface finish—a literature survey and discussion. Precis Eng 1988;10(4):215–20. https://doi.org/10.1016/0141-6359(88)90056-6.
[40] El-Axir M. An investigation into roller burnishing. Int J Mach Tool Manufact 2000;40(11):1603–17. https://doi.org/10.1016/S0890-6955(00)00019-5.
[41] Denkena B, Abrão A, Krödel A, Meyer K. Analytic roughness prediction by deep rolling. J Inst Eng Prod 2020;14(3):345–54. https://doi.org/10.1007/s11740-020-00961-0.
[42] de Oliveira DA, Martins AM, de Castro Magalhães F, Abrão AM. Characterization of the topography generated by low plasticity burnishing using advanced techniques. Surf Coating Technol 2022;448:128891. https://doi.org/10.1016/j.surfcoat.2022.128891.
[43] ASTM-G99-17. Standard test method for wear testing with a pin-on-disk apparatus. American Soc Test Mater 2017;3(2):1–6. https://doi.org/10.1520/G0099-17. ICS Code: 17.040.20.
[44] Grzesik W, Brol S. Wavelet and fractal approach to surface roughness characterization after finish turning of different workpiece materials. J Mater Process Technol 2009;209(5):2522–31. https://doi.org/10.1016/j.jmatprotec.2008.06.009.
[45] Gražulis S, Merkys A, Vaitkus A. Crystallography open Database (COD). Springer International Publishing; 2018. https://doi.org/10.1007/978-3-319-42913-7_66-1.
[46] Birkholz M, Fewster PF, Genzel C. Thin film analysis by X-ray scattering. Wiley-VCH Verlag GmbH & Co. KGaA; 2006.
[47] Degena T, Sadki M, Bron E, König U, Nénert G. The HighScore suite. Powder Diffr 2014;29(Supplement S2):S13–8. December 2014.
[48] Vogel MG, Sparks DL. Chapter 1 - the impacts of x-ray absorption spectroscopy on understanding soil processes and reaction mechanisms. In: Singh B, Gräfe M, editors. Synchrotron-based techniques in soils and sediments, vol. 34. of Developments in Soil Science, Elsevier; 2010. p. 1–26. https://doi.org/10.1016/S0166-2481(10)34001-3.
[49] Salvat F, Parellada J. Theory of conversion electron mössbauer spectroscopy (cems). Nucl Instrum Methods Phys Res Sect B Beam Interact Mater Atoms 1984;1(1):70–84. https://doi.org/10.1016/0168-583X(84)90481-6.
[50] Brand R. Normos mössbauer fitting program. Germany: Normos Program, Univ. Duisbg.; 2002. URL, https://www.uni-due.de.
[51] Gong J, Miao H, Peng Z, Qi L. Effect of peak load on the determination of hardness and young's modulus of hot-pressed si3n4 by nanoindentation. Mater Sci Eng, A 2003;354(1):140–5. https://doi.org/10.1016/S0921-5093(02)00940-1.
[52] Beausir B, Fundenberger J-J. Analysis tools for electron and x-ray diffraction. ATEX-software, Université de Lorraine - Metz; 2017. URL, www.atex-software.eu.
[53] Hertz H. Ueber die berührung fester elastischer körper. J für die Reine Angewandte Math (Crelle's J) 1882;1882(92):156–71. https://doi.org/10.1515/crll.1882.92.156.
[54] Korzynski M. Modeling and experimental validation of the force–surface roughness relation for smoothing burnishing with a spherical tool. Int J Mach Tool Manufact 2007;47(12):1956–64. https://doi.org/10.1016/j.ijmachtools.2007.03.002.
[55] Bouzid W, Tsoumarev O, Saï K. An investigation of surface roughness of burnished aisi 1042 steel. Int J Adv Des Manuf Technol 2004;24(1):120–5. https://doi.org/10.1007/s00170-003-1761-4.
[56] Li FL, Xia W, Zhou ZY, Zhao J, Tang ZQ. Analytical prediction and experimental verification of surface roughness during the burnishing process. Int J Mach Tool Manufact 2012;62:67–75. https://doi.org/10.1016/j.ijmachtools.2012.06.001.
[57] Sartkulvanich P, Altan T, Jasso F, Rodriguez C. Finite element modeling of hard roller burnishing: an analysis on the effects of process parameters upon surface finish and residual stresses. J Manufact Sci Eng, Transactions of the ASME 2007;129(4):705–16. https://doi.org/10.1115/1.2738121.
[58] Dzionk S, Dobrzynski M, Ścibiorski B. Jumping wave characteristic during low plasticity burnishing process. Materials 2021;14(6). https://doi.org/10.3390/ma14061441.
[59] Salahshoor M, Guo Y. Surface integrity of biodegradable magnesium–calcium orthopedic implant by burnishing. J Mech Behav Biomed Mater 2011;4(8):1888–904. https://doi.org/10.1016/j.jmbbm.2011.06.006. special Issue Soft Tissues.
[60] Angel T. Formation of martensite in austenitic steels. J Iron Steel Inst 1954;177:165–74.
[61] Greenwood NN, Gibb TC. Mössbauer spectroscopy. 1st ed. Springer Dordrecht, University of Leeds; 2011. https://doi.org/10.1007/978-94-009-5697-1.
[62] Brooks JS. Topics in applied physics vol 5 : Mössbauer spectroscopy. Phys Bull 1976;27(5):218. https://doi.org/10.1088/0031-9112/27/5/033.
[63] Gary LJ, Fernande G. Mössbauer spectroscopy applied to magnetism and materials science. 1st ed. New York, NY: Springer; 2013. https://doi.org/10.1007/978-1-4899-2409-4.
[64] Axinte DA, Gindy N. Turning assisted with deep cold rolling—a cost efficient hybrid process for workpiece surface quality enhancement. Proc IME B J Eng Manufact 2004;218(7):807–11. https://doi.org/10.1177/095440540421800713.
[65] Sunil S, Kapoor R. Effect of strain rate on the formation of strain-induced martensite in aisi 304l stainless steel. Metall Mater Trans A 2020;51:5667–76. https://doi.org/10.1007/s11661-020-05968-x.
[66] Xia P, Canillas Rodríguez FJ, Sabirov I. Microstructure evolution and adiabatic heating during dynamic biaxial deformation of a 304 stainless steel. Mater Sci Eng, A 2020;793:139829. https://doi.org/10.1016/j.msea.2020.139829.
[67] Andrade-Campos A, Teixeira-Dias F, Krupp U, Barlat F, Rauch EF, Grácio JJ. Effect of strain rate, adiabatic heating and phase transformation phenomena on the mechanical behaviour of stainless steel. Strain 2010;46(3):283–97. https://doi.org/10.1111/j.1475-1305.2008.00572.x.
[68] Martins AM, Leal CA, Campidelli AF, Abrão AM, Rodrigues PC, Magalhães FC, et al. Assessment of the temperature distribution in deep rolling of hardened aisi 4140 steel. J Manuf Process 2022;73:686–94. https://doi.org/10.1016/j.jmapro.2021.11.052.
[69] Sohrabi MJ, Mirzadeh H, Sadeghpour S, Mahmudi R. Grain size dependent mechanical behavior and trip effect in a metastable austenitic stainless steel. Int J Plast 2023;160:103502. https://doi.org/10.1016/j.ijplas.2022.103502. https://www.sciencedirect.com/science/article/pii/S0749641922002790.
[70] Brol S, Grzesik W. Continuous wavelet approach to surface profile characterization after finish turning of three different. Adv Manufact Sci Technol 2009;33(1):45–57.
[71] Fujimura Nao, Nakamura Takashi, Takahashi Kosuke. Changing mechanisms of surface relief and the damage evaluation of low cycle fatigued austenitic stainless steel. MATEC Web Conf 2018;165:04007. https://doi.org/10.1051/matecconf/201816504007.